Shape Analysis Based Strategies for Evaluation of Adaptations in In Vivo Right Ventricular Geometry and Mechanics as Effected by Pulmonary Hypertension

by

Jing Xu

Bachelor of Engineering, Southeast University, 2013

Submitted to the Graduate Faculty of

the Swanson School of Engineering in partial fulfillment

of the requirements for the degree of

Doctor of Philosophy

University of Pittsburgh

2020

UNIVERSITY OF PITTSBURGH

SWANSON SCHOOL OF ENGINEERING

This dissertation was presented

by

Jing Xu

It was defended on

February 20, 2020

and approved by

John C. Brigham, Ph.D., Professor, Department of Engineering Durham University

Jeen-Shang Lin, Ph.D., Associate Professor, Department of Civil and Environmental Engineering

Vikas Khanna, Ph.D., Associate Professor,Department of Civil and Environmental Engineering

Timothy Wong, Ph.D., Associate Professor of Medicine, Division of Cardiology

Dissertation Director: John C. Brigham, Ph.D., Professor, Department of Engineering Durham University

Shape Analysis Based Strategies for Evaluation of Adaptations in In Vivo Right Ventricular Geometry and Mechanics as Effected by Pulmonary Hypertension

Jing Xu, PhD

University of Pittsburgh, 2020

Pulmonary hypertension (PH) is a deadly disease, which as it progresses over time alters many aspects of the afflicted heart, and particularly the right ventricle (RV), such as its size, shape, and mechanical material properties. However, due to the limitations of what can be measured noninvasively in a standard clinical setting and the difficulty caused by the intrinsic complexity of the human RV, there has been little success to-date to identify clinically obtainable metrics of RV shape, deformation, or material properties that are quantitatively linked to the onset and progression of PH. Towards addressing this challenge, this work proposes the use of the shape and shape change of the RV, which is measurable from standard clinical imaging, along with statistical analysis and inverse material characterization strategies to identify new metrics of RV mechanical function that will be uniquely predictive of the state of the heart subject to PH. Thus, this thesis can be broken into two components: the first is statistical shape analysis of the RV, and the second is inverse characterization of heart wall mechanical material properties from RV shape change and measurable hemodynamics. For the statistical shape analysis investigation, a custom approach using harmonic mapping and proper orthogonal decomposition is applied to determine the fundamental components of shape (i.e., modes) from a dataset of 50 patients with varying states of PH, including some without PH at all. For the inverse characterization work, a novel method was developed to estimate the heterogeneous properties of a structure, given only the target shape of that structure, after a known excitation is applied to deform the structure. Lastly, the inverse characterization algorithm was extended to be applicable to actual *in vivo* cardiac data, particularly through the inclusion of a registration step to account for the organ-scale rotation and translation of the heart. Future work remains to expand on the computational efficiency of this inverse solution estimation procedure, and to further evaluate and improve upon the consistency and clinical interpretability of the material property estimates.

Table of Contents

List of Tables

List of Figures

Preface

Firstly, I would like to express my sincere gratitude to my advisor Prof. Brigham for providing tremendous support of my Ph.D. study and related research as well as the great support as my best friend while studying abroad while I was facing any problems no matter in research or in life. To me, he is the best mentor, best friend and best advisor in the world that I could imagine.

Besides my advisor, I would like to thank the rest of my thesis committee: Prof. Jeen-Shang Lin, Prof. Khanna Vikas, and Dr. Timothy Wong, for their insightful comments and encouragement, but also for the hard question which incented me to widen my research from various perspectives.

I want to express my deepest thanks to my mom and my dad, they motivated me a lot to stick with the original will to pursue the truth while I felt hesitated and lost directions in the research.

Last but not least, I would like to thank Dr. Zupan, Ellie Desmond who are my colleagues in the research group providing selfless help on my research path.

1.0 Introduction

Pulmonary Hypertension (PH) is a severe cardio-pulmonary illness affecting a wide range of people in all ages and racial populations, which has a significant affect on the mechanics of the heart. One of the most critical issues in the study and treatment of PH is that there is limited capability to judge both the early stages of this deadly disease, as well as the likelihood of progression to heart failure. PH is known to affect the size and shape, as well as the material properties of the heart, particularly the right ventricle (RV). As such, the mechanical functional state of the RV is thought to be a major determinant of symptoms and survival rates for PH. Although this natural and common hypothesis that the *in vivo* RV mechanics are important to better understanding PH, advances in utilizing this information have been relatively limited. There has been little success to-date to identify clinically obtainable metrics of RV deformation or material properties as a means to detect the onset and progression of PH. One likely significant limiting factor is that while some aspects of cardiovascular mechanics can be measured and/or estimated well, there is currently no trusted, clinically applicable method to accurately and consistently quantify the mechanical properties of the human RV *in vivo*. Towards addressing this challenge, this work develops and evaluates two parallel strategies to quantify RV mechanical function and its relationship to PH. The first strategy seeks to quantify the shape of the RV and to statistically evaluate the relationship between this shape and the state of PH, including the potential for heart failure. The second strategy seeks to quantify the mechanical material properties (e.g., elasticity) of the RV wall from clinically obtainable *in vivo* imaging and hemodynamic measurements by developing a novel inverse material characterization approach.

The statistical shape analysis component utilized a previously developed computational framework for the quantitative analysis and statistical decomposition of sets of 3D non-uniform and irregular shapes that combines a harmonic mapping approach directly with proper orthogonal decomposition. This analysis approach was applied to a unique 50-patient clinically obtained dataset considering the RV endocardial surface (RVES) at two points within the cardiac cycle, end diastole and end systole. The particular focus of this work was

to identify any and all features of the RVES shape that were statistically correlated to the traditional measures of the state of PH (e.g., hemodynamic measures, including pulmonary arterial pressure), and more importantly, the patient outcome, as defined by hospitalization with heart failure and/or death. The material characterization component required the development of a new strategy for inverse mechanical material property estimation that would be applicable to standard (e.g., untagged) medical imaging data and measurable excitation. To this end, an optimization-based inverse solution estimation algorithm was developed to estimate mechanical material properties by matching the shape change in an object due to a known excitation. This inverse solution estimation algorithm was first evaluated using simulated (i.e., *in silico*) inverse problems. Then, the inverse solution estimation algorithm was extended to be applicable to real clinical imaging data and hemodynamic measures that would be acquired for a standard patient with suspected PH. In particular, the algorithm included an approach to facilitate the use of simplified forward simulations of RV mechanics and efficiently and consistently evaluate general heterogeneity of the properties throughout the heart wall. The final inverse solution estimation algorithm was evaluated through application to two patient datasets, one with normal hemodynamic function and one with severe PH. The following chapters present the details of these methods and evaluates their effectiveness for the quantification of the *in vivo* mechanical properties of the human RV in relation to the state of PH.

2.0 Right Ventricular Feature Quantification by Shape Analysis Methods: Feasibility and Preliminary Associations with Clinical Outcome

Statistical shape analysis techniques are applied to a unique clinically obtained dataset to identify distinguishing features of the right ventricle (RV) shape as related to hemodynamic and outcome data. The goals of this pilot study are to demonstrate the feasibility of this technique to generate unique shape modes describing the RV and describe preliminary associations with clinical outcomes for pulmonary hypertension (PH). Steady state free precession cardiovascular magnetic resonance cine imaging in the short axis were acquired from 50 patients, of whom 33 had a clinical diagnosis of PH, and contemporaneous right heart catheterization data was acquired for all patients. To define outcome, all-cause mortality and hospitalization for heart failure were determined by clinical chart review. RV endocardial borders were manually segmented, and three-dimensional RV surfaces were reconstructed at end-diastole and end-systole for all patients. Registration and harmonic mapping was then used to create a quantitative correspondence between all RV surfaces in the dataset, and proper orthogonal decomposition was performed to generate unique modes describing various shape features of the RV. The results show that the shape analysis techniques can derive unique descriptors of RV shape in the form of modes corresponding to specific physically meaningful features. More importantly, the modes are seen to quantify features of shape that had been previously only qualitatively noted to relate to progression of PH. These modes describing features of the RV shape are further shown to correlate with clinically relevant measures of RV status, as well as clinical outcomes. Overall, these results motivate and lay the groundwork for further validation in undifferentiated cohorts.

2.1 Introduction

Pulmonary Hypertension (PH) is a severe and progressive cardio-pulmonary illness with a high mortality and morbidity rate. PH describes high blood pressure in the arteries of the lungs from any cause and is defined by a mean pulmonary arterial pressure (PAP) of above 25 $mmHg$ at rest, as assessed by right heart catheterization [27]. The signs and symptoms of PH in its early stages may not be noticeable for months or even years, and if left untreated, the resultant cardiopulmonary disease can be deadly [18]. Moreover, despite significant advances in both pathogenesis and treatment of PH over the past decade, right ventricular (RV) failure remains the most common fatal pathway in PH and a clear indicator of where this is likely to occur does not currently exist. A further understanding of features associated with the transition from a pressure overloaded, adapted RV to a dilated and failing RV is required to help identify patients at risk of RV-related heart failure and match them with appropriate therapies [62].

The current gold standard for PH diagnosis, catheterization, is necessarily invasive and requires hospital inpatient admission. Questions have also been raised regarding the consistency and efficacy of right heart catheterization given the wide variation in methodologies employed across different clinical practices, and therefore there is scope for research into non-invasive alternatives. The ongoing advancement and increased availability of three-dimensional (3D) image-based techniques such as cardiac magnetic resonance (CMR) and 3D echocardiography enables faster and more accurate assessment of RV structure noninvasively. However, at present these techniques are primarily used to quantify the size and function of the RV, and do not give fine structural detail [1], nor are they used in diagnosis. A recent review found that simple cardiac function indicators achieved by commonplace non-invasive procedures allowed only approximate estimation of right heart catheterization-derived parameters [54], and the current medical consensus is that CMR can be helpful in the diagnosis of PH only when used in conjunction with other techniques, including right heart catheterization and echocardiography [31, 27]. It is, however, accepted that the development of more advanced imaging tools will increase our understanding of the pathophysiological

features that contribute to RV failure in PH [31]. Developing a reliable, clinically-accepted, non-invasive gold-standard for PH diagnosis would be a landmark in automated disease diagnostics.

PH noticeably alters the shape and function of the RV. For example, the RV experiences hypertrophy in response to increased PAP, and this causes a flattening of the base of the ventricle [59, 60]. The hypertensive RV is also more spherical and has increased cross-sectional area at the mid and basal ventricular segments. Unfortunately, the complex shape and structure of the RV poses a challenge to traditional two-dimensional imaging, and consequently, compared to the left ventricle (LV), there have been few studies characterizing RV shape and function, and no long-term studies on the relation of the RV to relative patient outcome. Yet, a series of different measurements have been explored to study the change in RV shape and function in patients suffering from PH.

RV shape parameters, such as geometric shortening, have been associated with PH prognosis [42] and Vonk-Noordegraaf et al. [63] showed that right heart failure is related to functional adaptation of the RV. CMR studies have identified a significant difference between longitudinal and circumferential RV systolic function in PH [43]. Fernandez-Friera et al. [23] noted that apical right ventricular dysfunction occurred even in the presence of a normal global right ventricular ejection fraction (RVEF) in patients with PH. Moreover, the basal segments of the right ventricle showed either no change or a slightly increased end-systolic volume, implying some degree of compensation to maintain normal global RVEF. There have been additional attempts to characterise RV shape change and to identify relationships between the extent of geometrical alteration and the degree of pathology [38, 70, 2]. For example, Leary et al. [38] identified an RV shape common to PH which is typified by greater eccentricity and bulging at the base and apex of the ventricle.

Although several studies on RV shape and function clearly exist, the majority only calculate shape parameters, without comprehensive shape analysis. Alternatively, more recent efforts have attempted to used more generalized statistical and machine learning strategies to explore the relationship between PH and RV shape and function. In particular, Wu et al. [69] developed and evaluated a statistical shape analysis algorithm involving image alignment, topological mapping, and proper orthogonal decomposition to analyze RV shape features

and their dependence on the state of PH. Alternatively, Dawes et al. [20] used a supervised machine learning algorithm to determine if patient survival and mechanisms of RV failure in PH could be predicted using 3D patterns of systolic cardiac motion.

The knowledge on RV dysfunction in chronic pressure overload is progressing; however, there is still much to be understood. It remains unknown why some patients with severe PH are still able to maintain near normal cardiac outputs over a long period of time, while others experience rapid decompensation and death [17]. There are cases in which, despite mounting clinical evidence to show the presence of a change in RV shape and/or function suspected to be linked to pathological states, clinicians and scientists have been unable to find measurable, quantitative features that can discriminate the various states of pathology sufficiently to alter treatment methods and thus patient outcomes. The core hypothesis of the present work is that generalized quantitative analysis of RV shape and function could help in resolving these limitations in the diagnosis and prognosis of PH at an early stage. Using the framework established by Wu et al. [69] for statistical shape analysis of the RV, the aim of this study is to evaluate a unique dataset of clinically obtained CMR images and assess correlation of the shape features extracted from the RV with a range clinical measurements and patient outcome. Thereby, this work seeks to establish a baseline hypothesis for the predictive capability of shape features of the RV to estimate the state of PH and likelihood of adverse outcomes on which to build from with future large-scale patient studies. The following section briefly details the methodology of the statistical shape analysis and Section 2.3 details the clinically obtained dataset of CMR and other clinical measures utilized. Section 2.4 presents and discusses the results of the statistical shape analysis along with further statistical investigation of the significance of the shape features extracted in relation to the clinically obtained patient characteristics (e.g., hemodynamic measures) and adverse outcomes, which is followed by concluding remarks.

2.2 Methodology

The shape analysis framework used herein was developed by Wu et al. [69, 70, 68]. The overall workflow is shown in Figure 1. Given a dataset of medical images, first, a three-dimensional closed-surface representation of the shape of interest (the right ventricle in this work) is extracted, or segmented from each set of medical images. Next, the set of shapes are aligned/registered and a correspondence is established between each shape by topologically mapping each shape to a common reference domain. Lastly, the set of mapped shapes are statistically decomposed to identify a set of shape features and their corresponding significance for each shape in the dataset (i.e., coefficients).

2.2.1 Segmentation and Mesh Generation

The present work applied this shape analysis approach to assess variations in shape of the human right ventricle endocardial surface (RVES). The endocardial surface was chosen due to the relatively higher contrast of the blood-tissue boundary for the endocardial surface, which leads to this surface being extracted more accurately than the epicardial surface. The surfaces were obtained by manually segmenting the RVES from each imaging dataset, interpolating the slices, and then smoothing the interpolated surfaces using a standard recursive and discrete Gaussian filter within the commercial medical image processing software Simpleware (Synopsis Ltd., Exeter, UK). Manual segmentation was used to ensure that the most anatomically accurate representations of the RVES shape were segmented within the constraints of the medical image quality, and all segmentation was overseen by a trained cardiologist. Although details of the shape analysis framework are available in the references provided, the critical details of the remaining steps are given in the following for completeness.

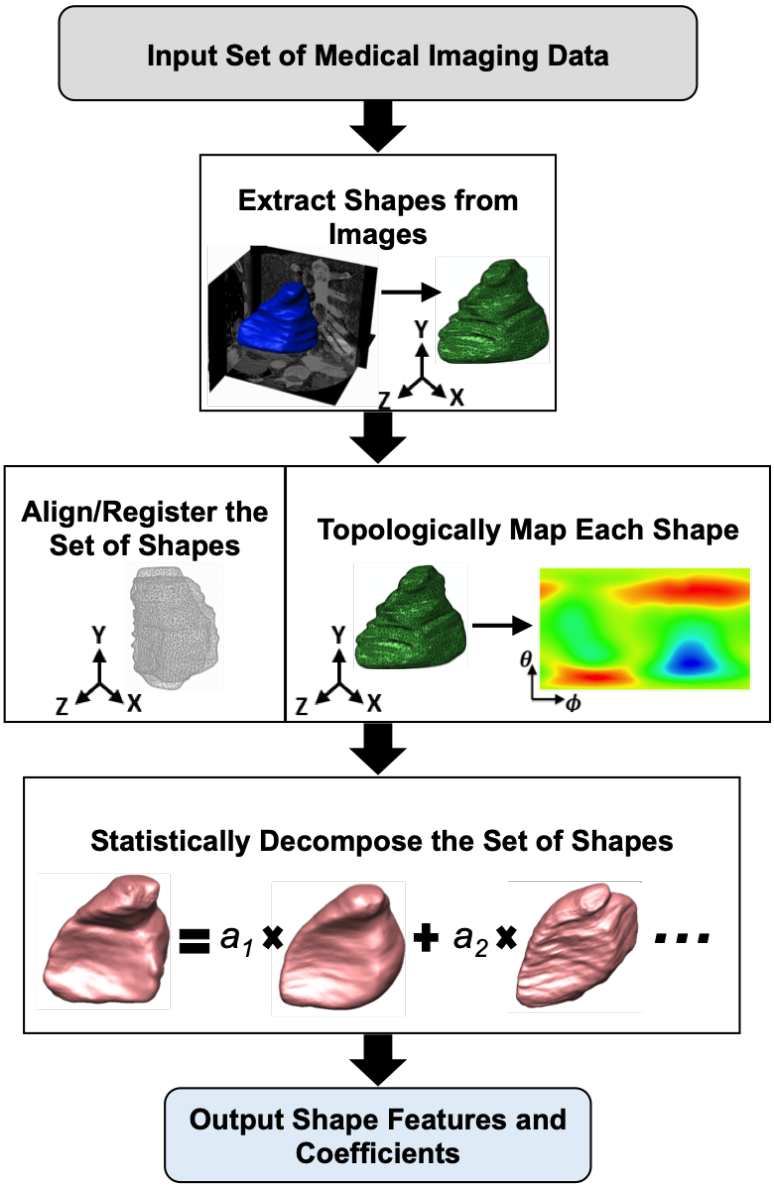

Figure 1: Overall statistical shape analysis procedure.

2.2.2 Registration

An iterative closest point (ICP) rigid registration algorithm [9, 10] was applied in the present study to align the set of RVES shapes to remove the effects of organ-level size, orientation, and position from the shape analysis. The ICP method uses rotation and translation to match a specified model (i.e., template), in this case a randomly selected RVES from the dataset, by minimizing the sum of square errors between the points on the model and the data being registered to it. First, each RVES shape was normalized (i.e. scaled) with respect to its internal cavity volume. Then, a rotation tensor and translation vector were determined to align each RVES to the template.

2.2.3 Topological Mapping

A harmonic mapping method (described in Wu et al. [69]) was applied to create a correspondence between all RVES shapes in the dataset. This approach was chosen as it can build correspondence with relatively high anatomical consistency in contrast to alternate methods [68], particularly if the statistical decomposition is applied directly to the mapped shapes without further processing, as was done in this analysis. The harmonic mapping approach utilizes the fact that the closed RVES surface is topologically equivalent to a sphere, and each RVES can therefore be uniquely mapped to the surface of a unit sphere. As such, the correspondence between any three-dimensional location on the surface of a given RVES and the two-dimensional location on the unit sphere can be determined from the solution of the following two Laplace's equations, which give spherical coordinates, θ (latitude) and ϕ (longitude):

$$\nabla^2\theta(\vec{x}) = 0,\ \forall\ \vec{x} \in \Omega_k \qquad \nabla^2\phi(\vec{x}) = 0,\ \forall\ \vec{x} \in \Omega_k, \tag{2.1}$$

where $\Omega_k \subset R^3$ is the k^{th} continuous, 3D, non-overlapping closed RVES domain and $\vec{x}$ are the standard Cartesian coordinates with respect to the origin for the given surface. This harmonic mapping requires at minimum two reference points, the north pole (Γ_n)

and the south pole (Γ_s) for the latitude mapping and a reference line, referred to as the dateline (Γ_d), for the longitude mapping to define the boundary conditions for the Laplace's equation. As the dateline represents where the longitude passes 360 degrees, it has a non-unique mapped value on the sphere. Therefore, the surface is cut along the dateline to create two independent, non-overlapping boundaries: an east dateline (Γ_d)and a west dateline (Γ_d^o). The values of the spherical coordinates along these references are assigned as:

$$\theta = 0,\ \forall\ \vec{x} \in \Gamma_n, \quad \theta = \pi,\ \forall\ \vec{x} \in \Gamma_s, \quad \phi = 0,\ \forall\ \vec{x} \in \Gamma_d, \quad \phi = 2\pi,\ \forall\ \vec{x} \in \Gamma_d^o. \tag{2.2}$$

In choosing these boundary conditions to be anatomical reference points, the analysis can be considered anatomically consistent across the dataset. Thus, for the analysis herein the anterior border between the free wall and septum of the RV with endpoints at the intersection with the pulmonary valve and apex was used as the dateline, and the intersection points were the poles. The poles and dateline were selected manually, to again ensure the most anatomically accurate representation was obtained. In addition, standard finite element analysis was used to solve the Laplace's equations for each RVES.

After mapping, the one-to-one correspondence can be inverted so that any given RVES ($\vec{x} \in \Omega_k$) can be described continuously with respect to a common domain for all RVES as a shape function as:

$$\vec{x} = \vec{x}(\theta, \phi),\ \forall\ \theta \in [0, \pi] \text{ and } \phi \in [0, 2\pi]. \tag{2.3}$$

As such, every RVES in the dataset can be quantitatively compared in a consistent manner.

2.2.4 Statistical Decomposition

Prior work has shown that less common statistical decomposition methods, specifically independent component analysis (ICA) [67], can provide alternate interpretations of the

shape features important to a dataset that may be significant. However, the present study applied the far more common proper orthogonal decomposition (POD) approach. POD can be interchangeably referred to as principal component analysis (PCA) or Karhunen Loeve transform, but the term POD is used herein to emphasize its application to the continuous form of the mapped shape functions (rather than the discrete form typical of PCA) and the use of the method of snapshots, which is relatively common in POD. The form of decomposition applied assumes that any shape function from the dataset could be decomposed as follows:

$$\vec{x}_k(\theta,\phi) = \vec{x}_\mu(\theta,\phi) + \sum_{i=1}^{m} a_{ki}\ \vec{v}_i(\theta,\phi), \tag{2.4}$$

where the translation function, $\vec{x}_\mu$, was chosen to be the mean of all RVES shapes, and a_{ki} is the coefficient that best approximates the k^{th} shape function with the i^{th} mode, $\vec{v}_i$. POD identifies the basis (i.e. modes) that minimizes the average difference between each dataset and the best approximation of the dataset using the basis (i.e., projection onto the modes). As noted, the method of snapshots was applied to form an n-dimensional eigenvalue problem, where n is the number of shapes in the dataset, to be solved to identify the set of POD modes. The eigenvalue corresponding to each mode is a measure of the relative importance of that mode to reconstructing all shapes in the dataset. Therefore, a typical rule is to consider the modes with the largest corresponding eigenvalues, such that the summation of the eigenvalues of the modes considered is in the range of 99% of the total sum of all eigenvalues in the set.

2.3 Clinical Dataset

2.3.1 Data Acquisition

Patients referred for clinically indicated cardiac imaging and right heart catheterization were prospectively enrolled in an observational study approved by our Institutional Review Board. Both procedures were performed on the same day or 1 day apart from each other. Cardiovascular magnetic resonance (CMR) was performed by dedicated CMR technologists on a short-wide bore 1.5-Tesla Siemens Magnetom Espree (Siemens Medical Solutions, Erlangen, Germany) equipped with a 32-channel cardiac coil. Standard breath-held cine imaging was acquired with steady-state free precession in the short axis orientation spanning the base to apex (6 mm slice thickness, 4 mm skip). Typical imaging parameters included 30 phases per R-R interval, matrix 256 by 144, flip angle 51 degrees, TE 1.11 ms, and acceleration factor 3. All images were deidentified prior to use.

2.3.2 Population Characteristics

A total of 50 patients were selected for analysis in this study. Table 1 summarizes the population characteristics that were considered. The presence of PH was defined by a mean pulmonary arterial pressure (PAP) greater than 25 $mmHg$. 33 patients were diagnosed with PH based on this criterion and 17 classified as Non-PH. Furthermore, there was a mixture of Group 1 (7 patients) and Group 2 (26 patients) within the PH cohort. Group classifications are described in Simonneau et al. [60], with Group 2 suffering from PH due to left heart disease as determined by a pulmonary capillary wedge pressure (PCWP) greater than 15 $mmHg$. Additional clinical measures assessed due to their potential link to PH included mean right atrial pressure (RAP), thermodilution estimate of cardiac index (THERCI), right ventricle ejection fraction (EF), brain natriuretic peptide (BNP), and patient age. It is important to note that this dataset is a dataset of convenience. Patients and their associated hemodynamic characteristics were extracted from previously collected clinical data rather

Table 1: Characteristics of the 50-patient population, divided by classification of diagnosed with pulmonary hypertension (PH) or without pulmonary hypertension (No PH), including mean pulmonary arterial pressure (PAP), pulmonary capillary wedge pressure (PCWP), mean right atrial pressure (RAP), thermodilution estimate of cardiac index (THERCI), right ventricle ejection fraction (EF), brain natriuretic peptide (BNP), and patient age, showing the mean value and the range in parentheses.

	PH (n=33)	**No PH (n=17)**
PAP ($mmHg$)	38.2 (28 - 71)	19.6 (11 - 25)
PCWP ($mmHg$)	20.3 (5 - 32)	10.6 (1 - 17)
RAP ($mmHg$)	14.0 (5 - 40)	4.9 (1 - 12)
THERCI ($L/min/m^2$)	2.5 (1.3 - 4.6)	2.8 (1.7 - 3.9)
EF (%)	40.6 (14.6 - 72.9)	56.4 (35.8 - 76.7)
BNP (pg/mL)	806 (14 - 3636)	445 (17 - 1249)
Age ($years$)	58 (18 - 79)	57 (28 - 79)

than a designed study. Thus, although 17 patients were not hypertensive, all patients had medical reason for evaluation for PH and none of the 50 patients would be classified as healthy.

Patients were also analyzed based on clinical outcome within 6 years of the date of image acquisition of mortality and/or hospitalization for heart failure (HHF) in one group and the remaining patients in the other. All cause mortality was determined by clinical chart review by staff supervised by both a PH specialist and general cardiologist. HHF was determined according to criteria utilized in prior studies [36]. Incident HHF required physician documentation of: (1) symptoms and physical signs consistent with heart failure, such as shortness of breath or rales, (2) supporting clinical findings, such as pulmonary edema on chest radiography, or (3) therapy for heart failure, such as diuretics. 10 patients from the cohort suffered HHF and 17 died, 4 of whom also suffered HHF, resulting in 23 total patients in the adverse outcome group.

Figures 2 and 3 show the classifications of the patients in terms of PH and outcome, respectively, with respect to the PAP and PCWP measures. Although more deaths occurred among patients with PH and a trend toward more HHF for patients with PH was observed as well, there is no clear correlation between the primary hemodynamic measures and patient outcome. This lack of clear correlation highlights the acknowledged challenge of predicting patient outcome using only standard clinical measures, particularly blood pressure alone.

2.4 Shape Analysis Results and Discussion

Statistical shape analysis was applied to each of the 50 patients at two phases of the cardiac cycle: end-systole and end-diastole, forming a total dataset of 100 shapes. The RVES shape at end-diastole of a patient in the cohort with normal hemodynamics was randomly selected as the template for the remaining 99 shapes in the ICP rigid registration process.

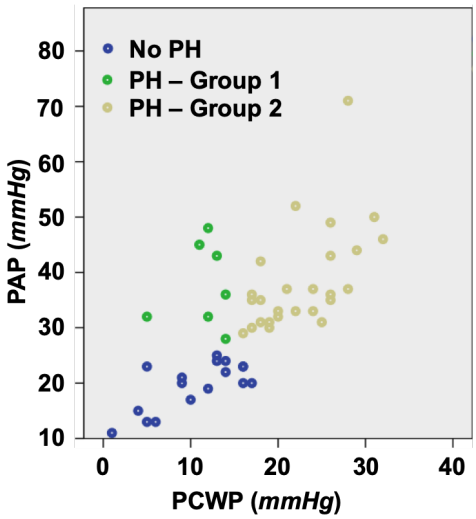

Figure 2: Classification of the patients in the dataset as being diagnosed as not having pulmonary hypertension (No PH), having Group 1 PH, or having Group 2 PH, with respect to the mean pulmonary arterial pressure (PAP) and the pulmonary capillary wedge pressure (PCWP).

2.4.1 Modal Decomposition

Figure 4 shows the cumulative modal energy (i.e., the ordered sum of the eigenvalues up to the corresponding mode number divided by the sum of all eigenvalues) of the 100 modes obtained from the statistical shape analysis. As is typical, based on the cumulative modal energy, a relatively small number of modes are necessary to capture the variation in shape throughout the dataset of 50 patient's RVES at end-diastole and end-systole. Only the first 6 modes are required to capture over 90% of the cumulative energy, the first 10 capture over 96%, the first 15 capture over 98%, and the first 20 capture over 99%. However, as the objective is to identify the shape features that relate to the state of PH and overall health, regardless of importance to overall shape reconstruction (i.e., regardless of whether the mode represents a relatively small component of the overall shape), it was necessary to consider more modes than would be necessary for accurate reconstruction. As such, in the following analyses the first 15 modes were retained and evaluated.

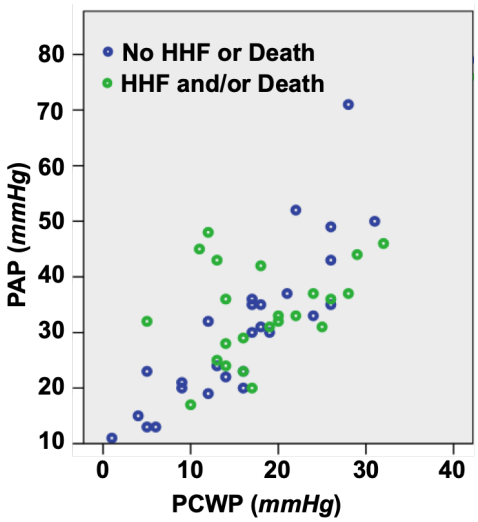

Figure 3: Classification of the patients in the dataset by outcome of having been hospitalized for heart failure and/or having died (HHF and/or Death) or having neither occur (No HHF or Death), with respect to the mean pulmonary arterial pressure (PAP) and the pulmonary capillary wedge pressure (PCWP).

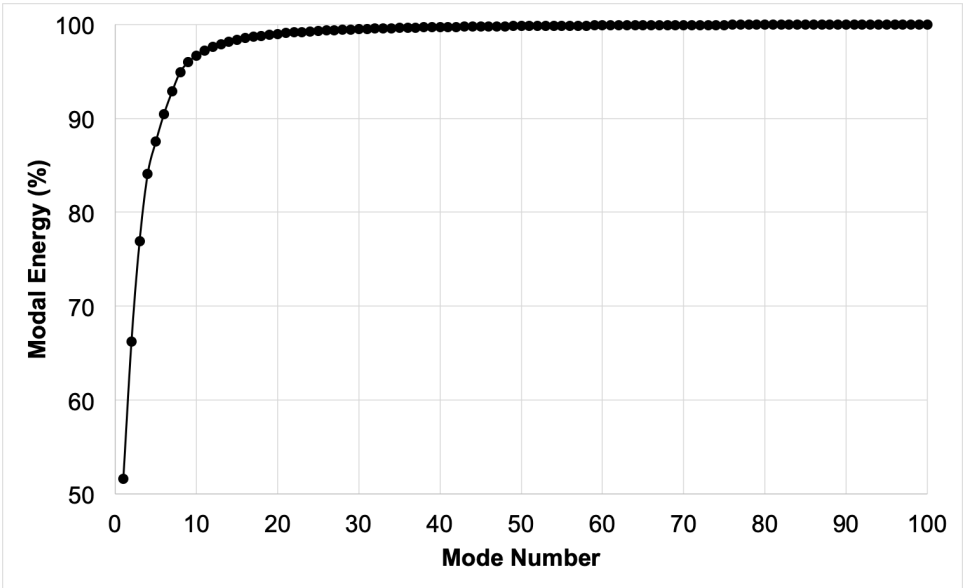

Figure 4: The cumulative modal energy corresponding to each of the RVES shape modes.

2.4.2 Significance of RVES Shape Modes in Predicting the State of PH

Pearson product moment correlation coefficients were calculated to determine whether any shape modes were significantly correlated with the state of PH, patient outcome, and hemodynamic variables. These Pearson values were calculated between each population characteristic variable and modal coefficients corresponding to each of the first 15 modes using the statistical analysis software IBM SPSS Statistics for Windows, version 26 (IBM Corp., Armonk, N.Y., USA). Initially, the statistical analysis was performed considering the modal coefficients for each patient's end-systole shape and end-diastole shape separately and combined as an average. This preliminary analysis showed a more significant correlation between the patient characteristics and the modal coefficients of each patient$\tilde{\text{O}}$s end diastole shape than the end systole shape or the two combined. Therefore, only the results for the end diastole modal coefficients are considered further herein.

Figure 5 shows a graphical representation of the resulting correlation matrix for the end-diastole shape modal coefficients and the patient characteristics. The absolute value of the correlation coefficients is shown to emphasize the strength of the correlation, without accounting for the direction of the correlation, making it easier to compare variables. Qualitatively, a clear correlation can be observed between the hemodynamic variables (PAP, RAP, PCWP, THERCI, and EF), and to a lesser extent, between the hemodynamic variables and BNP. Such results are expected as the hemodynamic parameters are physically linked to eachother. The only patient characteristic that appears significantly correlated with patient outcome is age, which again, is unsurprising as age is known to be strongly correlated with likelihood of dying in a given year [24]. With regard to the modal coefficients, some modes are significantly correlated to each other, but relatively few show significant correlation to any of the patient characteristics. Of these, Modes 13 and 8 stand out in particular as relating to the state of PH. Mode 13 was significantly correlated with PAP (Pearson correlation $r_{48} = 0.424$, $p = 0.002$), PCWP ($r_{48} = 0.349$, $p = 0.013$), and THERCI ($r_{48} = -0.284$, $p = 0.045$). Most importantly, Mode 13 also had the highest correlation of all variables other than age with outcome ($r_{48} = 0.438$, $p = 0.001$). Alternatively, Mode 8 was not significantly correlated with outcome ($r_{48} = 0.209$, $p = 0.145$), but was correlated with the

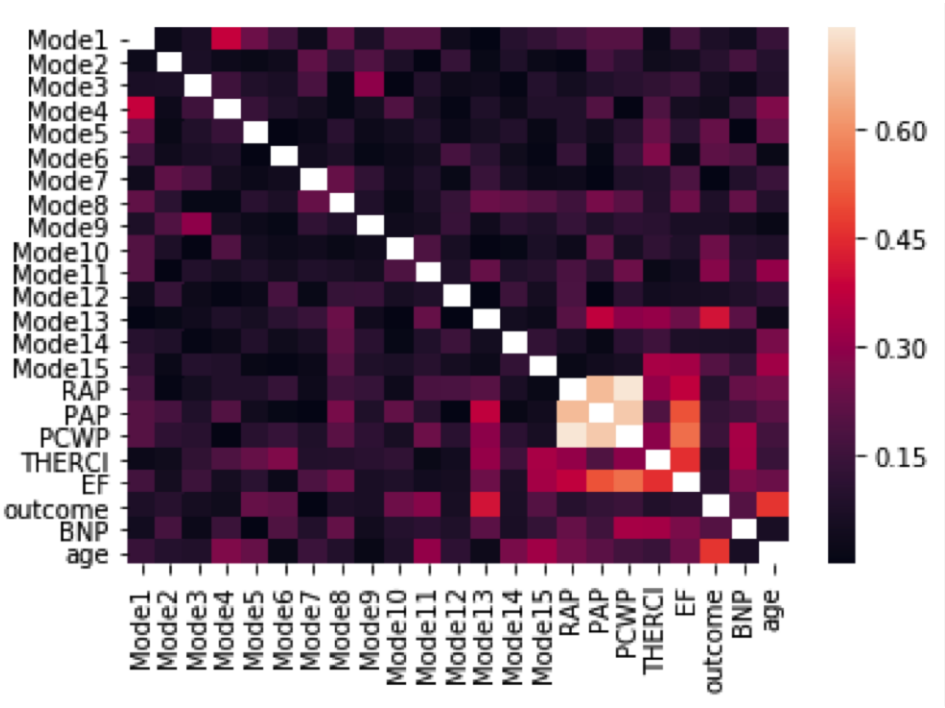

Figure 5: Absolute value of the magnitude of the Pearson correlation coefficient between each of the first 15 modal coefficients corresponding to the end-diastole shape and the patient characteristics.

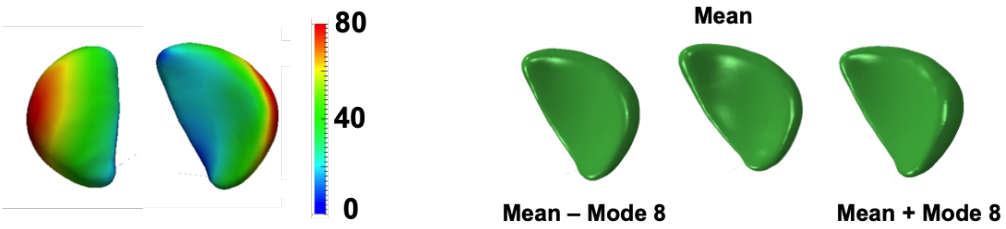

(a) (b)

Figure 6: (a) The free wall and septum view of the magnitude of mode 8 (color contours) plotted on the mean RVES shape and (b) the mean RVES shape with mode 8 subtracted, the mean RVES shape, and the mean RVES shape with mode 8 added.

hemodynamic variables used to classify the PH Groups: PAP ($r_{48} = 0.429$, $p = 0.002$) and PCWP ($r_{48} = 0.399$, $p = 0.004$). Additionally, Modes 8 and 13 were moderately positively correlated to each other ($r_{48} = 0.469$, $p = 0.001$), suggesting that the occurrence of a positive coefficient for Mode 8 also predicts a positive coefficient for Mode 13.

To interpret the relationship between the significant modes and RVES shape, Figures 6 and 7 show the effect of Modes 8 and 13, respectively, with regard to how they change the mean RVES shape. More specifically, the Figures show the spatial distribution of the shape change from the mean contributed by each mode as well as examples of the resulting change in the shape of the RVES by adding (i.e., having a positive corresponding coefficient) or subtracting (i.e., having a negative corresponding coefficient) each mode. It can be seen that Mode 8 contributes to an expansion of the free wall relative to the septum, such that a positive mode 8 coefficient leads to a rounder RVES, while a negative Mode 8 coefficient leads to a thinner RVES. Mode 13, meanwhile, affects more of the overall shape than Mode 8, clearly changing both free wall and septum. A positive Mode 13 coefficient appears to flatten the septum to produce a more 'D'-shaped RVES, while a negative Mode 13 coefficient appears to increase the crescent-like shape of the RVES.

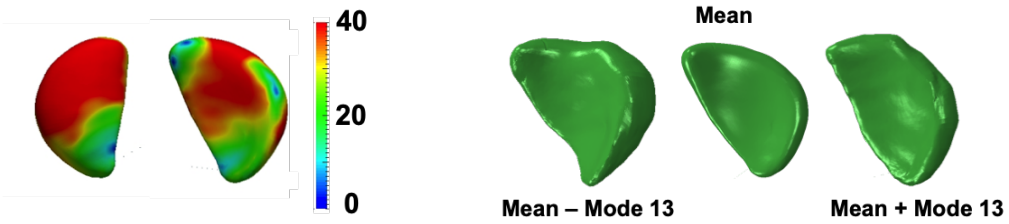

(a) (b)

Figure 7: (a) The free wall and septum view of the magnitude of mode 13 (color contours) plotted on the mean RVES shape and (b) the mean RVES shape with mode 13 subtracted, the mean RVES shape, and the mean RVES shape with mode 13 added.

2.4.2.1 Relationship between Shape and Existence of PH To examine the relationship between the two significant modes and PH, Figures 8 and 9 show PH classification with respect to PAP and the end diastole modal coefficient value for Modes 8 and 13, respectively. There is a distinct positive correlation between PAP and the coefficients of both modes. As such, patients with PH were significantly more likely to have a positive coefficient value corresponding to both Modes 8 and 13 and patients without PH were more likely to have a negative coefficient value for both modes. In other words, the heart of a patient with PH is more likely to have a rounder and more 'D'-shaped RVES, while a patient without PH is more likely to have a thinner, crescent-shaped RVES. These physical features are consistent with the long-standing clinical observation of the effects of PH to round out the RV and flatten the septum [63]. Thus, the statistical shape analysis was able to provide distinct features and quantitative measures of their appearance in any given heart that are well known (only qualitatively previously) to be determinant of a RV with PH. More importantly, with further development these shape features could potentially be used to quantitatively predict the presence of PH through imaging alone, and avoid the need for the current invasive hemodynamic measurement required to diagnose the condition.

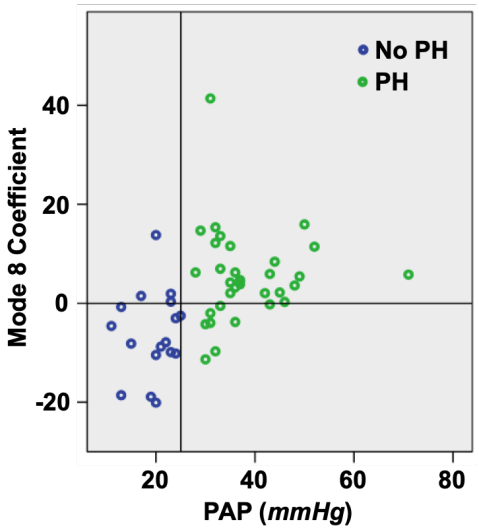

Figure 8: Mode 8 coefficient for the end diastole RVES shape and corresponding mean pulmonary arterial pressure (PAP) for each patient, as well as the classification as being diagnosed with pulmonary hypertension (PH) or not (No PH).

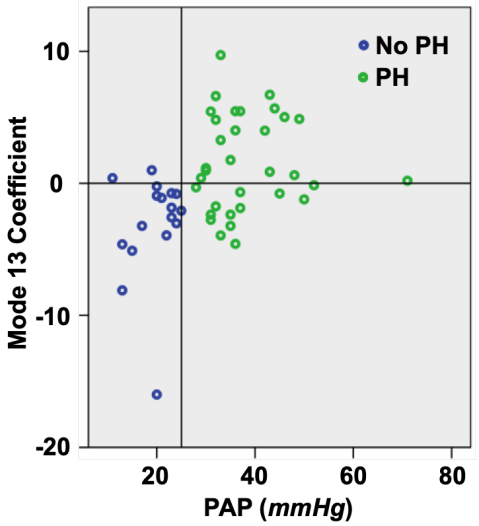

Figure 9: Mode 13 coefficient for the end diastole RVES shape and corresponding mean pulmonary arterial pressure (PAP) for each patient, as well as the classification as being diagnosed with pulmonary hypertension (PH) or not (No PH).

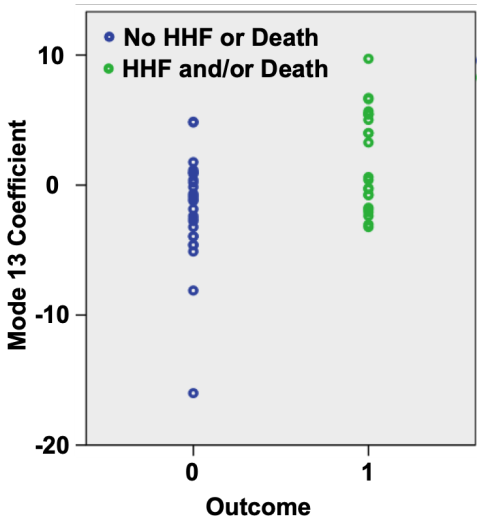

Figure 10: Mode 13 coefficient for the end diastole RVES shape and the classification by outcome of having been hospitalized for heart failure and/or having died (HHF and/or Death) or having neither occurred (No HHF or Death).

2.4.2.2 Relationship between Shape and Outcome Although a noninvasive predictor of PH would be significant, an even more important clinical need is to identify RV features that quantify whether a heart is adapting positively or negatively (i.e., leading to heart failure or death) to the presence of PH. This remains a major prognostic challenge using standard clinical measures, such as the patient characteristics shown herein. Thus, the relationship between modes and patient outcome was also explored.

Recall that the Mode 13 coefficient had the highest Pearson correlation coefficient with respect to outcome and that only one patient characteristic, age, exhibited a higher Pearson correlation coefficient than Mode 13. Figure 10 shows the patient outcome classification with respect to the end diastole modal coefficient value for Mode 13, and for comparison, Figure 11 shows the patient outcome classification with respect to PAP. Qualitatively, there is separation between the two outcome groups that is related to the Mode 13 coefficient value. There is also quantitative statistical evidence that patients with a larger Mode 13 coefficient are more likely to suffer an outcome of HHF and/or death (t-test statistic $t_{47} = 3.390$,

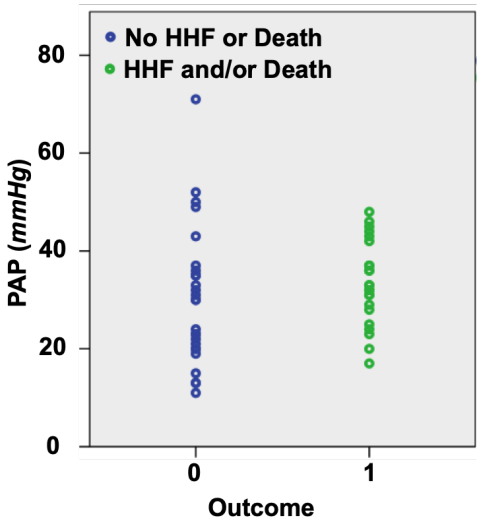

Figure 11: Mean pulmonary arterial pressure (PAP) and the classification by outcome of having been hospitalized for heart failure and/or having died (HHF and/or Death) or having neither occur (No HHF or Death).

$p = 0.001$). As such, there is clear potential for this shape feature to be used as a quantitative measure of RV adaptation and to contribute to predicting the likelihood of patient mortality or heart failure. In contrast, there is much greater overlap between the recorded PAP of the two outcome groups and there is no significant statistical evidence that patients with elevated PAP were more likely to suffer an adverse outcome ($t_{43} = 0.959$, $p = 0.343$). Overall, these results indicate that the statistical shape feature defined by Mode 13 provides an enhanced understanding of PH, over and above what can be gleaned from hemodynamic measures and can potentially assist in non-invasive diagnosis and prognosis of patients with PH.

2.5 Conclusions

A statistical shape analysis strategy was applied to determine shape modes/features associated with RV status and the adverse outcomes of HHF or death in patients with

PH. Two modes were highlighted as being significantly related to RV status with PH, and one mode in particular was identified as potentially being a unique quantitative predictor of outcome of HHF or death in diseased individuals. A relationship between RV shape and PH has been observed before, but this is the first time that a 3D statistical shape analysis approach has so clearly quantified this relationship. Specifically, the two shape modes highlighted were shown to define the change of a RV from relatively thin and crescent-shaped (i.e., healthy) to having an expanded free wall and flattened septum (i.e., unhealthy), which is commonly observed to be a more pathological state and is significantly correlated to increased PAP. Moreover, the division between the two outcome groups was greater for one of the shape modal coefficients than for any other measure available from the dataset other than age, including the hemodynamic measures PAP and PCWP, which are used in clinical diagnosis of PH. Thus, there is significant evidence to motivate further evaluation of the relationship between RV shape as quantified by shape analysis and the state of PH, and also to believe that non-invasive shape analysis can positively contribute to the timely and accurate diagnosis and prognosis of PH.

3.0 A Shape-based Strategy for Inverse Estimation of Soft Tissue Mechanical Material Properties from Untagged Medical Imaging Data

A computational approach is presented and evaluated to estimate the *in vivo* magnitude and spatial distribution of mechanical material properties of soft tissues. In particular, this strategy utilizes an optimization-type inverse problem solution procedure with a shape-based objective function to estimate the difference between the measured and predicted tissue behavior and estimate mechanical properties from standard untagged clinical imaging data. A set of simulated inverse problems are shown to evaluate the inverse solution estimation procedure based on estimating the passive elasticity of the human right and left ventricle wall from standard cardiac imaging data and corresponding hemodynamic measurements. Results show that the proposed shape-based approach can accurately estimate mechanical material properties, although the accuracy is dependent on the spatial region considered and their relative stiffnesses. The solution accuracy is also shown to be tolerant to the presence of model error. Moreover, additional tests show that the accuracy of the material property estimate of a priority region of the structure of interest can be improved, while simultaneously desensitizing the solution to additional model error by selecting an appropriate portion of the response shape to use within the objective function.

3.1 Introduction

The mechanical material properties of tissues have long been used, both qualitatively and quantitatively, as measures to determine both the presence and progression of a wide range of diseases. For example, the stiffening of breast tissue is a relatively well known indicator of the presence of abnormal tissue relating to cancer [11, 47], but there are many less common examples, such as the bladder [48], where mechanical properties are similarly important. In the cardiovascular system, aneurysms developed in the aortic or cerebral arteries show distinctly different mechanical properties in comparison to healthy arteries [56]. Moreover,

for the heart, it has been shown that the material properties of the right ventricle free wall are indicative of the progression of pulmonary hypertension [63], while other work has shown that material stiffness can be used as a potential predictor of the presence of left ventricle myocardial infarction [22, 34]. Based on these observations, there have been many studies to extract and mechanically test various tissues *ex vivo* to evaluate their properties and how they change in the presence of disease. Typical testing approaches for soft tissues include uniaxial or biaxial stretching devices [57, 34] and indentation tests [15], among others. However, to truly understand the effect disease has on the actual properties of tissues inside the body and to be able to use these properties for disease diagnosis and prognosis, it is critical that at least relative property changes can be identified quantitatively for tissues *in vivo*.

Some approaches to *in vivo* characterization of tissue properties can directly process the measurement signal to produce an estimate of material properties. These approaches include the wave-based techniques in which transient waves are generated in the tissue and the wave speeds or other dynamic properties are estimated from measurements of the tissue response, which can then be directly related to tissue mechanical properties [37]. However, these direct techniques are generally only applicable when the excitation applied is relatively controlled (e.g., to produce a shear wave) and may be limited to relatively simple material properties and assumptions for boundary conditions so that a reasonably accurate analytical relationship can be developed/used for the tissue response. Alternatively, model-based inverse problem solution strategies, and particularly partial differential equation (PDE)-constrained optimization approaches have become some of the most prevalent for tissue characterization applications, likely due to their generalized capability to account for complex and varying geometries, boundary conditions, and material models [8, 39, 72]. These optimization-based approaches generally cast the inverse problem as a constrained optimization problem to minimize an objective functional that quantifies the difference between the observed and estimated response of the tissue. Examples of optimization-based approaches include work to characterize arterial wall properties [25], to characterize skin material properties [12], and to estimate material properties of musculo-skeletal tissues [3], among others.

There are many different variations in the implementation of optimization-based methods that depend on the particular challenges of the tissues or organ being evaluated and the

available measurement information. These variations include the method of estimating the system response (e.g., solving the PDE in the boundary value forward problem) for a given set of property estimates, strategies to parameterize and regularize the unknown material properties, and the approaches to process the available measurements of the tissue response and the associated formulation of the objective functional to quantify the difference between that response and the estimated response. The present study is particularly focused on the use of available measurement information, with the success of inverse estimation strategies universally being directly linked to the quality and quantity of data that can be obtained non-invasively.

Many methods for *in vivo* tissue characterization have used direct measures of the primary variable in the forward problem within the objective functional, such as the displacement of portions of the tissue [49], or other direct measurable quantitates that are linked to the tissue displacement, such as surrounding fluid pressure [13]. For the case of *in vivo* tissue displacement, there are several strategies of measurement based upon medical imaging technology. For example, doppler ultrasound techniques have been used to measure the dynamic displacement responses at one or more spatial points throughout a tissue [53]. However, doppler ultrasound is generally limited to a relatively small amount of spatial information (i.e., only a relatively small number of points within a tissue domain can be measured). To obtain a more spatially complete measurement of tissue displacement, other studies have used either speckle tracking with ultrasound imaging [58] or magnetic resonance imaging with tagging [5]. Both speckle tracking and tagged imaging can provide approximate tissue displacement with high spatial resolution (e.g., they can be used to estimate full-field spatial response). Such spatially dense information can be especially useful to estimate spatially distributed material properties with relatively high accuracy and computational efficiency [64]. Yet, there are currently limitations in applying these full-field displacement measurement techniques for three-dimensional reconstruction (i.e., they are largely only applied to two-dimensional slices). Moreover, a different strategy is needed to use data without tagging or speckle tracking capability, either to evaluate historical data or even prospective imaging datasets from facilities that are not equipped with the state-of-the-art imaging tools.

An alternate approach to acquire the necessary measurement information of the tissue response for the inverse solution estimation is to apply a technique to process standard medical images (i.e., untagged and no speckle tracking) to estimate the displacement/deformation of the tissue being evaluated. Typically, these approaches will use some type of fiducial points on the tissue/organ of interest and/or simply develop a point-wise image-based correspondence between sequential images of the tissue/organ in time during excitation. Then, the displacement or deformation field can be approximated by assuming all corresponding points are the same material point in the tissue and interpolating between the points as needed. Examples of algorithms that estimate the tissue response this way include work to approximate the regional material properties of the heart wall from an estimated strain field throughout the heart acquired by applying a data fusion strategy to cardiac magnetic resonance images [66]. Alternatively, the work by Affagard et al. [3] used digital image correlation with ultrasound imaging data to estimate the displacement field for mechanically loaded thigh muscle, which was then used to approximate the material properties in several areas of the thigh. However, a concern for pre-processing approaches to first estimate the tissue displacement or deformation is that they potentially create additional error in the response measurement, noting that noise/error in measurements can have a disproportionate effect on the inverse solution estimation accuracy (i.e., can be a problem due to inverse problem ill-posedness). Alternatively, to ensure accuracy in the response estimation, it may be required to have relatively high temporal resolution with the imaging, limiting applicability to those cases. Lastly, the pre-processing simply adds another possibly time-consuming step to the inverse solution routine, and it would therefore be potentially beneficial to more directly utilize the available imaging information.

This paper presents and evaluates an approach to directly use what can be directly measured from clinical imaging data, which is the shape of the organ/tissue structure. By using shape as the comparison target in the optimization-based inverse problem solution routine, the only pre-processing of the imaging data necessary is to segment the shape of the organ/tissue structure of interest at the available time points during excitation. Section 3.2 briefly details the overall PDE-constrained optimization strategy to inversely estimate material properties, particularly focusing on the shape-based objective functional. Section 3.3

evaluates the capability of the inverse solution estimation algorithm to accurately estimate material properties. This work chose to use the exemplar case of evaluating passive elastic material properties of the heart wall assuming intraventricular pressure is known and using standard cardiac magnetic resonance imaging data to define the heart geometry and form the optimization objective functional. Although real human imaging data was used to generate the forward models of the heart used in the examples, *in silico* testing was used to evaluate the inverse solution capabilities, whereby the target heart shapes for the optimization objective functional were generated with the forward model with additional model error to provide realism. The presentation and discussion of the examples is followed by concluding remarks and suggestions for future studies.

3.2 Inverse Material Characterization Algorithm

3.2.1 PDE-Constrained Optimization

This work uses a standard strategy for estimating the solution to an inverse material characterization problem by casting the problem as a PDE-constrained optimization problem. As such, the inverse solution was estimated from the following optimization problem:

$$\begin{aligned} \underset{\vec{\gamma}}{\text{minimize:}} \quad & J\left(S_{est}(\vec{u}), S_{target}\right) \\ \text{subject to:} \quad & F(\vec{u}, \vec{\gamma}) = 0 \\ & \vec{b}_l \leq A(\vec{\gamma}) \leq \vec{b}_u, \end{aligned} \tag{3.1}$$

where J quantifies the difference between the shape of the object estimated from the solution of the PDE constraint equations (i.e., the governing equations of the physical system), S_{est},

and the given actual/target shape of the object being evaluated, S_{target}, $F(\vec{u}, \vec{\gamma})$ represents the PDE constraint equations, and A is the constraint operator to define the lower, $\vec{b}_l$, and upper, $\vec{b}_u$, bounds on the vector of unknown material parameters, $\vec{\gamma}$.

There are a wide range of strategies that have been developed to address various aspects of this optimization problem, particularly as different applications will have significantly different challenges/restrictions, which are often highlighted by the inherent ill-posedness of inverse problems. Variations exist for the specific formulation of the objective function, implementation of constraints, including how the forward problem (i.e., PDE-constraint) is solved, parameterization and regularization of the inverse problem unknowns, and the minimization strategy, and all of these variations can have a significant effect on the consistency and accuracy of the inverse solution estimate. The main focus of the present study is on the implementation and evaluation of a shape-based objective functional, which is detailed in the following section. Standard finite element analysis was used to solve the forward problem and the interior point gradient based optimization algorithm [14] with basic finite difference gradient estimation was used for the minimization. Additional details of the forward model and optimization algorithm, as well as the parameterization of the material properties to be inversely estimated are provided with the description of the example problems in Section 3.3.

3.2.2 Shape-Based Objective Functional

This work assumes that one or more surfaces of the organ or tissue region of interest can be extracted (i.e., segmented) from medical imaging datasets for a corresponding known or estimated stimulus (e.g., blood pressure) to serve as the inverse problem target shape. Surfaces were chosen rather than volumes due to the possibility that limitations in imaging may only allow for accurate extraction of a single surface (e.g., the inner wall of the heart, where the blood boundary is often easier to extract). Yet, it should be noted that a volume of tissue could be utilized by simply targeting both the inner and outer surfaces, provided they could both be accurately extracted from the imaging. Therefore, the minimization algorithm will search for material properties for the corresponding forward problem so that the shape of the organ or tissue region estimated by the forward problem "best" matches

the target surface shape(s). Of critical importance is that the direct use of shape eliminates the need to preprocess the data using additional assumptions (i.e., potentially adding error) about the response of the system to estimate a measure of displacement or deformation to use as the inverse problem target.

There are several approaches to represent shape that could potentially be applied to quantify the difference between the target shape and that estimated by the forward problem for the organ or tissue region of interest [73] . For this study to evaluate the concept of a shape-based objective, a modified version of one of the more commonly used contour-based strategies was used, the Hausdorff distance [21]. A modification of the Hausdorff distance was chosen, not only because of the relatively frequent use of Hausdorff distance in shape comparison/matching applications, but also because of its intuitive nature and ease of implementation. The Hausdorff distance is a point-to-point matching (i.e., correspondence-based) method, and the specific version used finds the maximum of the average of the closest pairings between all the points on each shape. Applying this modified Hausdorff distance and assuming each shape can be discretized into a set of points in cartesian space, the objective for the PDE-constrained optimization problem can be written as:

$$J\left(S_i, S_j\right) = \max\left(M\left(S_i, S_j\right), M\left(S_j, S_i\right)\right) \tag{3.2}$$

with

$$M\left(S_i, S_j\right) = \frac{1}{N_i} \sum_{n=1}^{N_i} \min_{\vec{p}_m^{\,j} \in S_j} \left\| \vec{p}_n^{\,i} - \vec{p}_m^{\,j} \right\|, \tag{3.3}$$

where N_i is the total number of discrete points in the i^{th} shape, $\vec{p}_n^{\,i}$ is the vector of cartesian coordinates for the n^{th} point on the i^{th} shape, and $\| \cdot \|$ is the standard Euclidean distance operator. This modified version of the Hausdorff distance can be thought of as similar to

an l_2-norm for the comparison of two shapes, which is significant as it takes into account all parts of the shapes in contrast to the standard Hausdorff distance that is more similar to an l_∞-norm and estimates the maximum difference between two shapes.

3.3 Examples and Discussion

A series of simulated inverse problems to characterize the material properties of the heart ventricular wall were considered. More specifically, the nonlinear elastic material parameters were estimated for the left and/or right ventricles of the heart utilizing the shape change of the endocardial surfaces of the ventricles from end systole to end diastole, assuming the response was entirely passive and driven by the intraventricular pressure (i.e., effects of flow were assumed to be negligible). Therefore, endocardial surfaces extracted at end diastole were used as the target shape(s) for the optimization procedure. Only the endocardial surface was used for the shape targets to mimic the common reality that this surface can be estimated significantly more accurately from the imaging data than any other portion of the organ due to the blood boundary contrast. This work assumes that the passive response of the heart could be sufficiently estimated using a bi-ventricle model that combined only the right and left ventricle of the heart. Although a considerable simplification of the geometry, single-ventricle [40, 6] and bi-ventricle [51, 55] models have been commonly used in prior studies examining heart wall mechanics. Assuming the end systolic geometry of the heart is the reference/unstressed state is also noted to be a significant simplification. However, this simplification is consistent with similar work to estimate heart mechanical properties [6], where it is noted to be a beneficial choice to ensure consistency and solution identifiability in comparison to alternate choices of times in the cardiac cycle. It should also be noted that the methods proposed for the inverse characterization procedure would not change in any way with a more complex forward model.

Although actual human imaging data was used to create the initial forward problem geometry at end systole, the target end diastole shapes were simulated using the forward model with chosen material properties. This work focuses on simulated inverse problems

to numerically evaluate the solution capabilities of this shape-based strategy to understand the capability to obtain consistent and accurate solution estimates for the material properties. A particular focus is on the affect the data amount and quality has on the inverse characterization capability.

3.3.1 Bi-ventricle Forward Model

A patient was randomly selected from a clinically obtained dataset of cardiac magnetic resonance (CMR) images from the University of Pittsburgh Medical Center to create the bi-ventricle geometry. The chosen patient had normal hemodynamics and normal cardiac function as assessed by a clinical cardiologist. Images were acquired using a 1.5-Tesla Siemens Magnetom Espree (Siemens Medical Solutions, Erlangen, Germany) equipped with a 32-channel cardiac coil. Standard breath-held cine imaging was acquired with steady-state free precession in the short axis orientation spanning the base to apex (6 mm slice thickness, 4 mm skip). Typical imaging parameters included 30 phases per R-R interval, matrix 256 by 144, flip angle 51°, TE 1.11 ms, and acceleration factor 3.

To create the starting geometry, the right and left ventricular walls were manually segmented from all slices from approximately the basal plane to the apex at the phase approximating end systole for the chosen patient. The geometry was smoothed with a standard recursive Gaussian smoothing filter and meshed with 4-node tetrahedral elements using the commercial image processing software Simpleware [1]. Standard convergence tests were performed to ensure the mesh size was sufficiently small for accurate simulation. Additionally, the geometry was somewhat arbitrarily divided into three regions to investigate the effect of heterogeneity, with the regions associated as: the right ventricle free wall, the left ventricle free wall, and the septum. Figure 12 shows the top view (i.e., basal plane) of the bi-ventricle geometry, including the three regions specified.

The support conditions included restricting the entire basal plane to have zero displacement in the transverse (i.e., axial) direction. In addition, the inner (i.e., endocardial) boundary of the basal plane of the left ventricle was arbitrarily chosen to have zero displacement in

[1] (www.simpleware.com)

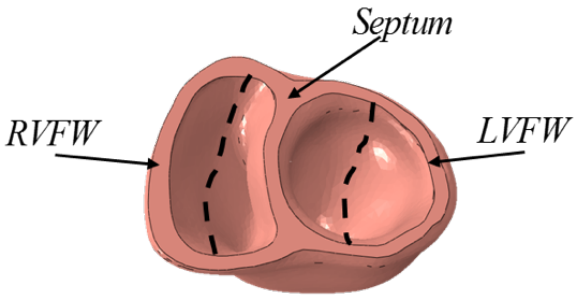

Figure 12: Bi-ventricle geometry with the divisions according to the dashed black line into the right ventricle free wall (RVFW), the left ventricle free wall (LVFW), and the septum regions.

all directions to prevent rigid body motion and to ensure the model was not overly flexible. To simulate the passive diastolic process and estimate the end diastole shape, intraventricular pressures in a typical range for end diastole were applied to the left and right ventricles. The pressures were applied uniformly to the inner wall surfaces with magnitudes of 12 $mmHg$ and 8 $mmHg$ for the left and right ventricles, respectively. As is discussed in the relevant results section, for a portion of the tests, model error was added to this applied pressures to test the capability to estimate the inverse problem solution with imperfect data.

A quasi-incompressible transversely isotropic version of the Fung model [32] was chosen for the bi-ventricle material. It should again be noted that the methods proposed for the inverse characterization procedure would not change in any way with a different constitutive model. The isochoric portion of the strain energy function for the chosen material model was defined as:

$$2\Psi(\mathbf{E}) = C_0 \left(e^{Q(\mathbf{E})} - 1\right) \tag{3.4}$$

with:

$$Q(\mathbf{E}) = b_1 E_{ff}^2 + b_2(E_{cc}^2 + E_{rr}^2 + 2E_{cr}E_{rc}) + b_3(E_{fc}E_{cf} + E_{fr}E_{rf}), \tag{3.5}$$

where $\mathbf{E}$ is the Green-Lagrange strain tensor, such that E_{ff} is fiber-direction strain, E_{cc} is the cross-fiber in-plane strain, E_{rr} is radial strain, and E_{cr}, E_{fr} and E_{fc} are the respective shear components of strain, and C_0, b_1, b_2, and b_3 are the unknown material parameters. To simplify the inverse problem, the relationship between nonlinearity parameters used in Genet et al. [29] was applied. Thus, given a fiber-direction parameter of $b_1 = B_0$, the transverse parameters were set to $b_2 = 0.4B_0$, and $b_3 = 0.7B_0$. Additionally, the fiber direction was manually applied to approximately coincide with the plane transverse to the thickness direction of the ventricular wall. Therefore, the inverse characterization procedure was applied to determine values for two parameters, the stiffness C_0 and the nonlinearity B_0, for each region of interest of the bi-ventricle model.

3.3.2 Coarse Sensitivity Analysis of Shape-Based Objective Function

A coarse sensitivity analysis was performed first to determine whether the Hausdorff distance would change significantly due to a significant change in the material parameter values and to qualitatively assess the error response surface. Target shapes for the left and right ventricle endocardial surfaces were generated using arbitrarily chosen base material parameters of $C_0 = 1.0\ kPa$ and $B_0 = 14.4$ for the right ventricle free wall and septum portions of the geometry and $C_0 = 1.15\ kPa$ and $B_0 = 16$ for left ventricle free wall portion of the geometry. The two material parameters were then incrementally varied, ranging by $\pm 50\%$ of the base values, for both stiffness parameter and nonlinearity parameter for each of the three regions, in turn, the forward problem was repeated for the varied parameters, and the Hausdorff distance between the target shapes and the corresponding shapes from the analysis with varied parameters was determined. Figures 13-15 show the average of the Hausdorff distances for the two ventricles obtained from modifying the material parameters

over the given ranges for the right ventricle free wall, the left ventricle free wall, and the septum, respectively, each while keeping the material parameters of the other two regions fixed at the base values. These local sensitivity plots of the Hausdorff distances with respect to the arbitrary base properties have nearly identical shapes for the variations of the three material property regions (right ventricle, left ventricle, and septum). The most noticeable difference is that the sensitivity of the response to changes in the left ventricle free wall region is significantly greater than the others, with the change in Hausdorff distance being almost double that of the other two regions for some parameter combinations. This increased sensitivity for the left ventricle is simply because the left ventricle is the largest portion of the bi-ventricle model by volume. Yet, in all cases the change in Hausdorff distance (i.e., inverse problem target error) is smooth and convex within the domain of parameter values explored. This is particularly important in the context of potential use of gradient-based optimization, with surfaces such as these expected to be easily traversed with an optimization algorithm to produce a solution with relatively low error using a relatively low number of iterations. However, although each sensitivity plot has a clear minimum of zero at the point corresponding to the base material parameters, each plot also has a distinct trough where the Hausdorff distance is relatively near to zero. The reason for these troughs is that variations in material parameters along the trough produce nearly identical strain energy functions for the range of deformation experienced by the heart during the diastolic process simulated.

The cause of the troughs in the error response surfaces can be seen further by considering two cases for parameters along the trough in the left ventricle material parameter response surface that are nearly identical in Hausdorff distance, but have significantly different parameter values, as shown in Table 2. Figure 16 shows the uniaxial fiber-direction Second Piola-Kirchhoff stress with respect to uniaxial fiber-direction Green-Lagrange strain based on the constitutive models with these two parameter combinations over a range of strain approximating the maximum experienced by the analyses of the diastolic process. As can be seen, although the parameters are significantly different, the stress-strain diagrams are nearly identical. Having inherently non-unique, or nearly non-unique parameter values with respect to the constitutive model can create issues with the optimization-based inverse solution estimation procedure, particularly for non-gradient-based methods that may be "confused" by

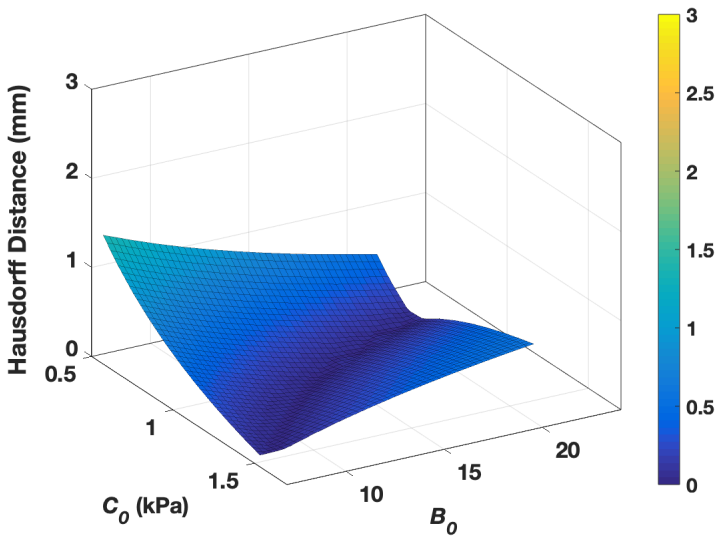

Figure 13: Average Hausdorff distance between the left and right ventricles at end diastole comparing to the ventricles with the base material parameters due to variations in the stiffness (C_0) and nonlinearity (B_0) parameters of the right ventricle free wall portion.

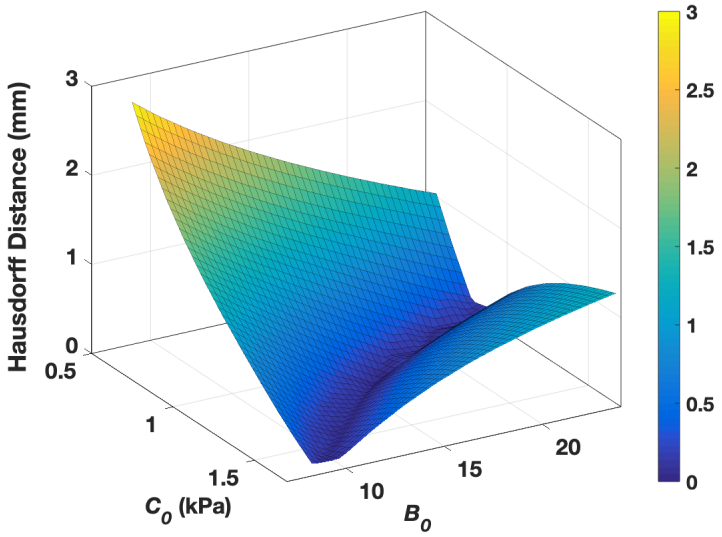

Figure 14: Average Hausdorff distance between the left and right ventricles at end diastole comparing to the ventricles with the base material parameters due to variations in the stiffness (C_0) and nonlinearity (B_0) parameters of the left ventricle free wall portion.

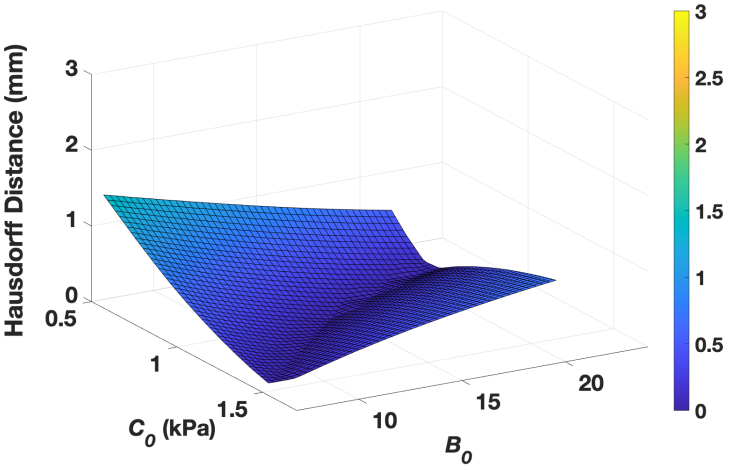

Figure 15: Average Hausdorff distance between the left and right ventricles at end diastole comparing to the ventricles with the base material parameters due to variations in the stiffness (C_0) and nonlinearity (B_0) parameters of the septum portion.

Table 2: Two cases of material parameters and their associated average Hausdorff distance for the left ventricle error response surface.

	$\mathbf{C_0}$ (kPa)	$\mathbf{B_0}$	**Hausdorff Distance** (mm)
Case 1	0.9	19.2	0.25
Case 2	1.4	14.4	0.26

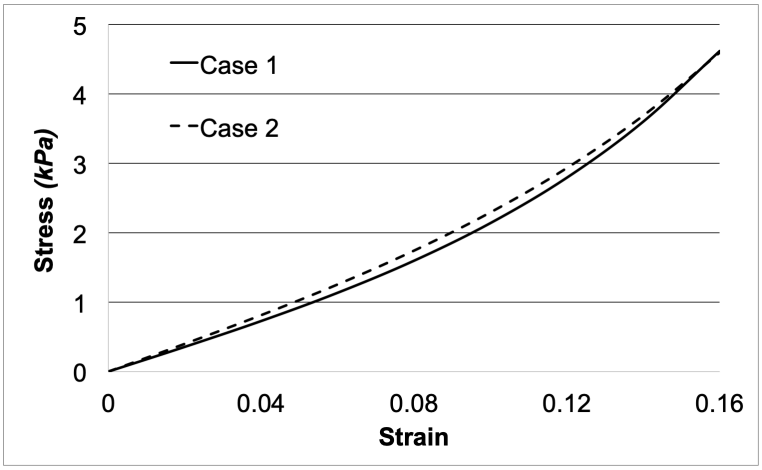

Figure 16: Uniaxial stress versus uniaxial strain corresponding to the two cases of material parameters from the trough region of the left ventricle material parameter response surface.

response similarity for disparate parameter values, leading to more iterations being required to achieve convergence. Moreover, any optimization may ultimately terminate early on non-ideal parameter values, particularly in the inevitable presence of model and measurement error for real systems. However, in practice, as long as the results are presented in terms of the constitutive model such as with stress-strain plots similar to Figure 16, rather than the parameter values alone, then the variations in material parameters can be mitigated as the constitutive model presentation would allow for consistent interpretation (including comparing results across different specimens) even if the parameters themselves did not. A similar example is the work by Brigham and Aquino [13], which showed that the equivalent elasticity and dissipation of a viscoelastic model could be recovered accurately over a finite frequency range through an optimization-based inverse solution strategy, even though the parameters defining the viscoelastic model were non-unique.

3.3.3 Inverse Material Characterization Targeting Both Left and Right Ventricle

The first set of simulated inverse problems utilized both the left and right ventricle endocardial surfaces for the target data by using the average of the respective modified Hausdorff distances as the optimization objective function, which was the same metric plotted for the sensitivity analysis. A series of test cases were considered, first assuming the bi-ventricle to be homogenous, and then assuming that the properties were discretely heterogeneous with different parameters for each of the three predefined regions. For each test, the optimization process was repeated five times, with a different randomly generated initial guess for the material parameters to evaluate the consistency of the inverse solution estimation. The material parameters were constrained based on the feasible ranges seen in prior studies to $C_0 \in [0.8\ kPa, 3\ kPa]$ and $B_0 \in [10, 30]$. For the homogeneous test case, the initial guesses were selected manually to ensure coverage of the parameter ranges, and for all other tests the initial guesses were generated using uniform distributions within the respective ranges. The stopping criteria for each optimization was when the Euclidean norm of the change in parameter values was less than 10^{-25} or the number of iterations exceeded 50.

For the homogeneous test case, the material parameters used to generate the target shapes were set to $C_0 = 1.15\ kPa$ and $B_0 = 16$. Table 3 shows the results of each of the five optimization trials, including the initial guesses for the parameter values and the parameter estimates when the optimization completed along with the corresponding minimum objective function value (i.e., average modified Hausdorff distance). Table 3 also shows the averages and standard deviations over the five trials for the solution estimates and the corresponding objective function values. Although the average parameter estimates were very near to the values used to generate the target data, with the average stiffness parameter in particular matching exactly with that used to generate the inverse problem target shape, the variability in the estimates across the five trials was substantial and clearly significantly dependent upon the initial guess for the solution. Yet, the corresponding final objective function values were all well within a magnitude that would be considered accurate in terms of shape matching, with the least accurate trial still producing an average modified Hausdorff distance of only 0.27 mm. To add context, the blood volume in the right ventricle considered at end diastole was approximately 205 mL, which would convert to a spherical diameter of approximately 7.3 cm. Therefore, the least accurate average modified Hausdorff distance was less than 0.4% of a representative internal dimension of a ventricle. Moreover, the parameters corresponding to the best final shape matching (Trial 1), which would be chosen as a final solution estimate, were actually farthest from the values used to generate the target data of all trials. These results further emphasize the importance of not relying on such non-unique parameters alone to interpret the inverse material characterization results.

To better interpret the inverse solution estimation results, Figure 17 shows the uniaxial fiber-direction stress with respect to uniaxial fiber-direction strain based on the constitutive models over a range of strain approximating the maximum experienced by the analyses with the parameter values used to generate the target data and the parameter values estimated by the optimization trial with the lowest objective function value (i.e., the best solution,

Table 3: Initial parameter estimates (Initial Guess), final solution estimates after optimization (Solution Estimate), and average modified Hausdorff distance for the solution estimate (Objective Function), as well as the average and standard deviations for the five trials of the test case with homogeneous material properties and targeting both the left and right ventricle shape for the inverse problem.

	Initial Guess		**Solution Estimate**		**Objective**
	$\mathbf{C_0}$ (kPa)	$\mathbf{B_0}$	$\mathbf{C_0}$ (kPa)	$\mathbf{B_0}$	**Function** (mm)
Trial 1	1.60	18.00	1.25	15.00	0.03
Trial 2	2.00	10.00	1.23	15.08	0.07
Trial 3	1.30	19.00	1.05	16.80	0.14
Trial 4	2.50	10.00	1.00	17.02	0.27
Trial 5	1.50	13.00	1.23	15.10	0.08
Average			1.15	15.80	0.12
Std. Dev.			0.12	1.02	0.09

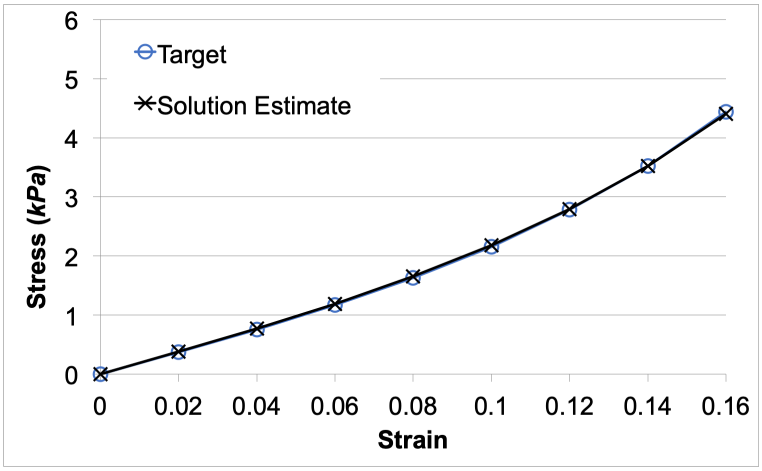

Figure 17: Uniaxial stress versus uniaxial strain corresponding to the material parameters used to simulate the inverse problem target data (Target) and the inversely estimated material parameters (Solution Estimate).

Trial 1). The two stress-strain plots are nearly identical, even though the parameter values are significantly different. To quantitatively compare the constitutive models, the relative L_2-error was calculated from the stress-strain plot as:

$$\text{Error in the Constitutive Model} = \frac{\|\mathbf{S}_{target}(\mathbf{E}) - \mathbf{S}_{est}(\mathbf{E})\|_{L_2}}{\|\mathbf{S}_{target}(\mathbf{E})\|_{L_2}}, \tag{3.6}$$

where $\|\cdot\|_{L_2}$ is the standard L_2-norm, which was applied over the range of the Green-Langrange strain shown of $[0, 0.16]$, and $\mathbf{S}_{target}$ and $\mathbf{S}_{est}$ are the Second Piola-Kirchhoff stresses as produced by the material parameters used to generate the target shapes and the material parameters estimated by the inverse solution procedure, respectively. The Error in the Constitutive Model corresponding to the stress-strain diagrams in Figure 17 was 0.7%, which quantitatively confirms that the constitutive models generated by the parameter sets over the range of strains experienced by the simulated heart are nearly identical.

To evaluate the capability to inversely estimate heterogeneous properties, the parameters were randomly modified to create three distinct sets for the three regions, resulting in 6 parameters to be inversely estimated. Table 4 shows the parameter values used to generate the target shapes, the initial guesses for the parameter values, the parameter estimates when the optimization completed, and the corresponding minimum objective function value. Similarly to the test case with homogeneous material properties, there was substantial variation in the material property estimates across the five optimization trials, with none of the trials producing parameter values particularly similar to the values used to create the target shapes for the inverse problem for the three regions of the bi-ventricle model. Yet, the average modified Hausdorff distance for all trials indicated accurate shape matching, and thus all feasible inverse solutions, with the average value being even lower than that for the homogeneous test case. To again better interpret these inverse solution estimation results, Figure 18 shows the uniaxial fiber-direction stress with respect to uniaxial fiber-direction strain based on the constitutive models with the parameter values used to generate the target data and the parameter values estimated by the optimization trial with the lowest objective function value (Trial 5) for all three regions of the bi-ventricle model. The material property estimate of the septum portion of the bi-ventricle model was clearly the most accurately estimated, with the accuracy for the septum similar to that for the previous homogeneous test case, while the accuracies of the left and right ventricle portions were significantly lower. The Error in the Constitutive Model (Equation 3.6) corresponding to these stress-strain diagrams were 13%, 39%, and 0.5%, for the left ventricle free wall, the right ventricle free wall, and the septum portions, respectively. The observed higher sensitivity for the left ventricle free wall portion of the bi-ventricle model response makes it not surprising that the left ventricle property estimate was relatively more accurate than the right ventricle property estimate. However, it is important to note that the absolute error for the right ventricle material property was lower than that for the left ventricle, but the relative error was higher as the target right ventricle properties were substantially smaller than the left ventricle properties. Overall, although the material property estimate accuracy for the left ventricle and right ventricle

Table 4: Parameter values used to generate the inverse problem target shapes (Target Values), initial parameter estimates (Initial), final solution estimates after optimization (Solution), and average modified Hausdorff distance for the solution estimate (Objective Function) for the left ventricle free wall (LVFW), right ventricle free wall (RVFW), and septum portions of the bi-ventricle model for the five trials of the test case with heterogeneous material properties and targeting both the left and right ventricle shape for the inverse problem.

	LVFW		**RVFW**		**Septum**		**Objective**
	$\mathbf{C_0}$ (kPa)	$\mathbf{B_0}$	$\mathbf{C_0}$ (kPa)	$\mathbf{B_0}$	$\mathbf{C_0}$ (kPa)	$\mathbf{B_0}$	**Function** (mm)
Target Values	3.00	16.00	1.00	14.00	1.15	16.00	
Trial 1							
Initial	1.49	10.36	2.06	14.22	2.23	17.43	
Solution	1.71	11.76	1.82	11.18	1.79	11.40	0.09
Trial 2							
Initial	2.17	18.49	1.12	19.16	3.19	13.92	
Solution	1.88	10.99	1.25	15.04	2.06	10.15	0.09
Trial 3							
Initial	3.19	19.34	3.08	17.92	2.01	16.55	
Solution	2.68	18.31	1.56	10.27	1.69	11.99	0.14
Trial 4							
Initial	3.21	16.79	2.38	19.59	2.80	11.71	
Solution	1.89	10.92	1.63	12.08	2.08	10.14	0.11
Trial 5							
Initial	1.04	16.56	2.84	11.42	1.19	17.58	
Solution	2.89	14.72	1.90	10.86	1.08	16.80	0.07

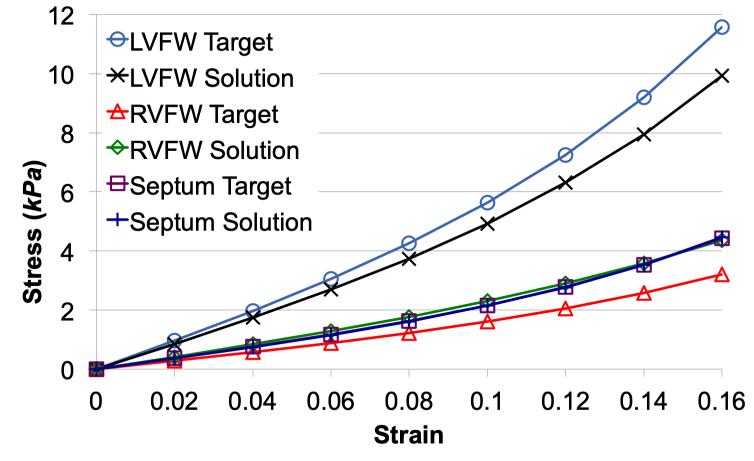

Figure 18: Uniaxial stress versus uniaxial strain corresponding to the material parameters used to simulate the inverse problem target data (Target) and the inversely estimated material parameters (Solution) for the left ventricle free wall (LVFW), right ventricle free wall (RVFW), and septum portions of the bi-ventricle model.

portions were lower than the septum, both were still relatively close to the target solutions, and of particular significance, the relative distribution of properties was maintained (i.e., the stiffer left ventricle portion and softer right ventricle portion were clearly identified as such).

3.3.4 Inverse Material Characterization Targeting Only Right Ventricle

The second set of simulated inverse problems was intended to explore the possibility that a significantly smaller portion of the structure of interest is the only portion that can be confidently extracted to serve as the inverse problem target and/or the properties of only a portion of the structure are required to be accurately estimated. The latter reason is relevant for applications such as the evaluation of adaptation of the heart due to pulmonary hypertension, which is generally hypothesized to significantly affect the right ventricle, but not the left ventricle (e.g., right ventricle properties would be desired from the inverse estimation, but not left ventricle) [41]. Thus, if the sensitivity of the properties that are not

important could be reduced without significantly affecting the sensitivity of the important properties, then the number of inverse problem unknowns could potentially be reduced, lowering computational expense and possibly improving the uniqueness of the solution. To test this capability, only the right ventricle endocardial surface was used for the target data, even though characterization of both ventricles was considered.

A coarse sensitivity analysis was again performed, following the same base material parameters and approach as was used in Section 3.3.2, but only quantifying the modified Hausdorff distance with respect to the shape of the right ventricle alone. The shapes of all of these local sensitivity plots were similar to the previous cases (Figures 13-15), including the convexity and the trough, so these are not shown here for brevity. What was most significant was the change in the magnitude of the sensitivity plots. The sensitivity for the septum portion of the bi-ventricle changed by a relatively small amount, with the maximum Hausdorff distance increasing from approximately 1.4 mm to approximately 1.5 mm by evaluating only the right ventricle shape. More importantly, with respect to the properties of the right ventricle free wall portion the maximum Hausdorff distance increased from less than 1.5 mm to over 2 mm, whereas with respect to the properties of the left ventricle free wall portion the maximum Hausdorff distance decreased from approximately 3 mm to approximately 2 mm. Thus, as was hoped, by only targeting the right ventricle shape, the sensitivity of the desired properties (the right ventricle free wall) were substantially increased, while the sensitivity of the undesired properties (the left ventricle free wall) were substantially decreased.

The same optimization procedure was used as was applied to the previous inverse estimation tests, including the five optimization trials for each target, the random generation of the initial guesses, the constraints, and the stopping criteria. However, for simplicity only the best solution (i.e., the solution with the lowest modified Hausdorff distance) of the five trials was examined for each test. All test cases utilized the heterogenous scenario, again seeking to determine two material parameters corresponding to each of the three regions (right ventricle free wall, left ventricle free wall, and septum). Additionally for this second set of tests, to avoid the inverse crime for the simulated inverse problems (i.e., to ensure the model used to generate the target data was different than the model in the inverse solution estimation

process) and test solution capabilities with imperfect data, tests were also performed for which the pressures applied to generate the target shapes were different than those used in the inverse estimation procedure. For the inverse estimation procedure, the pressures were applied uniformly as before with magnitudes of 12 $mmHg$ and 8 $mmHg$ for the left and right ventricles, respectively. However, to generate the target data for the modified tests, random "error" was added to the pressure magnitudes by dividing each ventricle inner wall into 4 sections and adding randomly generated error to the pressure applied to each section. Thus, the applied pressure for a given section was 12 $mmHg \times (1 + \eta)$ for the left ventricle and 8 $mmHg \times (1 + \eta)$ for the right ventricle, where η is a uniformly distributed random variable between 0 and 0.01. To assess the impact of this model error, the first simulated case also was considered with error-free target data as was done in the previous section (i.e., the target was generated with the uniform pressures). To evaluate the robustness, three additional test cases with arbitrarily chosen heterogeneous material properties were considered, all of which included the model error.

Table 5 shows the four parameter sets used to generate the target shapes for each of the four test cases, and the parameter estimates and corresponding minimum objective function value obtained from the best solution of the five optimization trials for each test case with the inclusion of model error, as well as the first test case without the inclusion of model error. The first test case without including model error was as accurate as the prior test cases for the new material property distribution in terms of the modified Hausdorff distance for the final inverse solution estimate. The inclusion of model error substantially increased this final solution error for the corresponding test case (Test 1) and each of the other three test cases obtained a final solution with a similar magnitude of error. Thus, the increase in shape-matching error was consistent with respect to the inclusion of model error, which should be expected since the simulation used for the inverse solution procedure could no longer exactly match the target shape of the right ventricle. Yet, the modified Hausdorff distances corresponding to all inverse solution estimates obtained were still substantially smaller than the overall size of a normal human heart, indicating that the shape matching could still be considered accurate.

Table 5: Parameter values used to generate the inverse problem target shapes (Target), the best solution estimates after optimization for the case without model error (No Error Solution) and all cases with model error (Solution), and average modified Hausdorff distance for the solution estimates (Objective Function) for the left ventricle free wall (LVFW), right ventricle free wall (RVFW), and septum portions of the bi-ventricle model for the four test cases with heterogeneous material properties and targeting only the right ventricle shape for the inverse problem.

	LVFW		**RVFW**		**Septum**		**Objective**
	$\mathbf{C_0}$ (kPa)	$\mathbf{B_0}$	$\mathbf{C_0}$ (kPa)	$\mathbf{B_0}$	$\mathbf{C_0}$ (kPa)	$\mathbf{B_0}$	**Function** (mm)
Test 1							
Target	1.15	16.00	3.00	16.00	3.00	16.00	
No Error Solution	1.64	12.22	3.08	15.52	3.10	15.48	0.08
Solution	1.33	17.05	3.00	17.44	2.26	19.00	0.24
Test 2							
Target	1.15	16.00	1.00	14.40	1.00	14.40	
Solution	2.05	10.76	1.28	12.65	1.60	10.24	0.40
Test 3							
Target	1.15	16.00	1.00	14.40	3.00	16.00	
Solution	1.34	15.07	1.68	10.35	2.88	17.34	0.32
Test 4							
Target	1.15	16.00	3.00	16.00	1.00	14.40	
Solution	1.04	19.84	2.37	19.92	1.31	10.42	0.34

Table 6: The Error in the Constitutive Model for the best solution estimates after optimization for the first case without model error (Test 1 No Error) and all test cases with model error for the left ventricle free wall (LVFW), right ventricle free wall (RVFW), and septum portions of the bi-ventricle model for the four test cases with heterogeneous material properties and targeting only the right ventricle shape for the inverse problem.

	LVFW	**RVFW**	**Septum**
Test 1 No Error	3 %	1 %	1 %
Test 1	25 %	12 %	6 %
Test 2	10 %	9 %	7 %
Test 3	8 %	13 %	7 %
Test 4	20 %	6 %	12 %

Table 6 shows the Error in the Constitutive Model corresponding to the stress-strain diagrams for each of the test results. Similarly to the prior tests, the variation in the relative error of the material property estimates correlates with the relative stiffness of the regions of the bi-ventricle model, with stiffer regions having relatively more accurate solution estimates. As would be expected, the material property estimate for the first test case without model error was substantially more accurate than the solution estimates for the test cases with model error. The effect of the model error was particularly significant on the accuracy of the material property estimate for the left ventricle free wall portion of the bi-ventricle model, which is consistent with the reduced sensitivity of the left ventricle portion when only targeting the right ventricle shape. Similarly, due to the targeting of the right ventricle shape alone, the accuracy of the material property estimates for the right ventricle free wall portion of the bi-ventricle model were more accurate on average than the prior cases targeting both ventricle shapes, while there was a corresponding decrease in the accuracy of the left ventricle free wall and septum portions. Yet, the overall accuracies of the material

Table 7: Parameter values used to generate the inverse problem target shape (Target), the best parameter solution estimates for the right ventricle free wall (RVFW) and the septum portions of the bi-ventricle model after optimization with the fixed erroneous left ventricle free wall parameters shown (LVFW), and average modified Hausdorff distance for the solution estimates (Objective Function) targeting the shape of both the left ventricle and right ventricle (Solution - LV and RV) and only targeting the right ventricle shape (Solution - RV) for the inverse problem.

	LVFW		**RVFW**		**Septum**		**Objective**
	$\mathbf{C_0}$ (kPa)	$\mathbf{B_0}$	$\mathbf{C_0}$ (kPa)	$\mathbf{B_0}$	$\mathbf{C_0}$ (kPa)	$\mathbf{B_0}$	**Function** (mm)
Target	1.15	16.00	3.00	16.00	3.00	16.00	
Solution - LV and RV	1.21	16.80	2.20	16.08	2.40	19.76	0.25
Solution - RV	1.21	16.80	3.10	15.44	3.15	15.03	0.12

property solution estimates for all cases targeting only the right ventricle shape, with and without model error, were not significantly decreased in contrast to the previous tests using the left and right ventricle shape as the inverse problem target.

As a last test, a trial was evaluated for which the two material parameters corresponding to the left ventricle free wall were fixed (i.e., removed as an inverse problem unknown) with erroneous values. The parameter error was approximately 5% and was in addition to the model error already included in the applied intraventricular pressure (i.e., the two sources of model error were combined). This test was intended to not only increase the model error, but examine the potential benefit of targeting only a portion of the shape to reduce sensitivity to the properties of a separate region of the structure (the left ventricle in this case) that are not considered important.

Table 7 shows the parameter values used to generate the target shape, the parameter estimates when the optimization completed (noting only 4 parameters were estimated corresponding to the right ventricle and septum), and the corresponding minimum objective function value. Additionally, Table 8 shows the Error in the Constitutive Model correspond-

Table 8: The Error in the Constitutive Model for the best solution estimates after optimization for the left ventricle free wall (LVFW), right ventricle free wall (RVFW), and septum portions of the bi-ventricle model targeting the shape of both the left ventricle and right ventricle (LV and RV) and only targeting the right ventricle shape (RV) for the inverse problem.

	LVFW	**RVFW**	**Septum**
LV and RV	12 %	26 %	6 %
RV	12 %	1 %	3 %

ing to the stress-strain diagrams for each of the test results. As was intended, the shape matching accuracy, in terms of the modified Hausdorff distance was considerably improved by only targeting the right ventricle endocardial surface rather than both ventricles, and the corresponding accuracy of the right ventricle free wall and septum material property estimates was substantially improved, particularly the right ventricle properties that went from relatively inaccurate to the most accurate of the three portions. As such, a clear benefit can be obtained by targeting only the portion of a shape that corresponds to a region of desired parameters, by not only potentially increasing the accuracy of the desired solution estimate, but decreasing the needed accuracy of the unimportant material properties.

3.4 Conclusions

An optimization-based inverse material property estimation procedure using a shape-based objective function applicable to evaluating the *in vivo* properties of tissues from untagged medical imaging data was presented and numerically evaluated. By constructing the objective function of the optimization procedure based on shape, the algorithm is able to more directly use standard clinical imaging data and avoid potential additional computing

cost and processing error needed to first estimate tissue displacement or deformation from the images. The inverse estimation procedure was evaluated through *in silico* tests with a bi-ventricle model based on actual cardiac geometry extracted from a clinically obtained human cardiac magnetic resonance imaging dataset. Inverse problems were simulated to evaluate the diastolic properties of the bi-ventricle model, in which the elastic material properties of the left ventricle free wall, the right ventricle free wall, and the interventricular septum were estimated. The algorithm was shown to be able to traverse the optimization search space to minimize the shape-based objective function and accurately reconstruct both homogeneous and heterogeneous material property estimates for the three sections of the heart. It was also shown that it is important to evaluate the solution estimate accuracy using the material model (e.g., stress-strain behavior) rather than the parameters themselves, as the parameters are non-unique. Overall, the regional accuracy was found to depend on the percentage of total volume accounted for by a region and the relative stiffness, with the stiffer regions generally more accurately estimated. The inclusion of model error in the simulated inverse problems was shown to decrease the accuracy of the estimated material properties, but no more so than would be expected and relatively accurate solutions could still be obtained when model error existed. Lastly, the relative accuracy of the regional property estimation was shown to be dependent upon the amount the structure's shape used for the optimization objective, with more accurate solutions to selected regions being obtained by using the shape of the corresponding region alone (i.e., using less information). Thus, for cases where the evaluation of one portion of the organ/structure is a priority, a useful strategy can be to increase the solution sensitivity for that region while decreasing the sensitivity of others by targeting the shape of the priority region alone with the inverse estimation procedure.

A particular focus of future work is to expand the clinical applicability of the shape-based inverse estimation algorithm, particularly for the purpose of estimating the *in vivo* mechanical material properties of the heart. A specific focus will be to improve the forward model to be more representative of the actual *in vivo* behavior of the heart within the inverse solution procedure, especially to account for the organ-level motion of the heart.

This extension will allow the inverse approach to be suitably applied to real target imaging data (e.g., the heart shape at end diastole extracted from medical images), and to validate its capability for further practical use.

4.0 A Clinically Applicable Strategy to Estimate the In Vivo Distribution of Mechanical Material Properties of the Right Ventricular Wall

A clinically applicable approach to estimate the in vivo mechanical material properties of the heart wall is presented. In particular, this optimization-based inverse estimation approach applies a shape-based objective functional combined with a registration strategy and incremental parameterization of heterogeneity to be capable of utilizing standard (i.e., untagged) clinical imaging data along with simplified representations of cardiac function as the forward model, and still provide consistent and physically meaningful solution estimates. The capability of the inverse estimation algorithm is evaluated through application to two clinically obtained human datasets of cardiac magnetic resonance imaging and associated intraventricular pressure measurements to estimate the passive elastic mechanical properties of the heart wall, with an emphasis on the right ventricle. One dataset corresponded to a patient with normal heart function, while the other corresponded to a patient with severe pulmonary hypertension, and therefore expected to have a substantially stiffer right ventricle. For these tests, patient-specific pressure-driven bi-ventricle finite element analysis was used as the forward model and the endocardial surface of the right ventricle was used as the target data for the inverse problem. By using the right ventricle alone as the target of the inverse problem the relative sensitivity of the objective function to the right ventricle properties is increased. The results show that the inverse solution estimation method is able to identify properties to accurately match the corresponding shape of the simplified forward model to the clinically obtained target data, and the properties obtained for the example cases are consistent with the clinical expectation for the right ventricle. Additionally, the material property estimates indicate significant heterogeneity in the heart wall for both patients, and more so for the patient with pulmonary hypertension.

4.1 Introduction

As is the case for many diseases and the associated organs or tissues that are affected by them, the mechanical material properties of the heart have been found to vary significantly in the presence of a wide range of cardiac illnesses [33, 19, 63, 22]. Therefore, the ability to estimate changes in such properties is often hypothesized to be a predictive measure for the state and/or progression of disease. Pulmonary hypertension (PH) is one particular deadly cardio-pulmonary illness, which is clinically characterized by a haemodynamic state of elevated mean pulmonary arterial pressure [35], that has been shown to significantly change the mechanical properties of the right ventricle (RV) of the heart in particular [62]. For example, the work in Trip et al. [61] showed that a measure of bulk (i.e., organ-level) diastolic stiffness of the RV in humans, measured by post-processing the pressure-volume loop, is correlated to PH severity. Alternatively, the work by Hill et al. [34] evaluated the mechanical change at the tissue-level of the RV due to PH through *ex vivo* studies using a rat model of the disease.

Although, a link between the mechanical material properties of the tissue of the RV wall and PH appears to exist, investigation using human data is limited due to the challenges of *in vivo* estimation of the material properties of the heart in general. A fundamental challenge of this problem, and any similar *in vivo* characterization problem, is the limitations of available measurement data. For the case of PH [27, 26], clinically available information for a given patient may include standard (i.e., untagged) cardiac magnetic resonance imaging (MRI) stacks that can be used to reconstruct an estimate of the three-dimensional shape of the heart at various points in the cardiac cycle (often 10-20) and right heart catheterization measurement of the corresponding intraventricular pressure throughout the cardiac cycle. Thus, full understanding of the excitation (i.e., hemodynamics) is not known, which is a potential source of error, and direct measurement of displacement/deformation, which is often the measurement information used for a mechanical characterization problem, is not available. Such challenges are relatively common for *in vivo* estimation of any tissue

properties, and yet, over the years there have been several research efforts to develop techniques for *in vivo* estimation of mechanical material properties (e.g., elastic material parameters) of the heart wall.

Due to the described limitations in measurement information, analytical or other direct approaches to estimate the solution to the inverse problem of characterizing the heart wall properties are normally intractable. Therefore, a common inverse solution procedure implemented has been to cast this inverse characterization problem as an optimization problem. In this optimization-based approach the material properties are estimated by minimizing a measure of the difference between the heart deformation derived from the medical imaging and that estimated by a simulation of the heart deformation that depends upon the material properties. One example of an optimization-based inverse characterization approach for the heart wall is the work by Asner et al. [6] that estimated active and passive mechanical properties for a left ventricle (LV) model of the heart by minimizing the difference between a finite element representation of the LV response over a cardiac cycle and the displacement of the LV wall and cavity pressure estimated from experimental measurements. Gao et al. [28] similarly characterized passive mechanical material parameters for the LV by minimizing the difference between the measured chamber volume and strain values in the heart wall and those estimated by a finite element representation. Although the majority of studies to-date have focused on the LV, and thus, only included the LV geometry in the forward model similarly to the previous references [7, 45, 29, 44, 52, 46, 65], some work has considered ventricular interaction and characterized properties for more than just the LV [66, 50, 55]. For example, the work by Wong et al. [66] used a bi-ventricle model that included both the LV and RV combined, and characterized material properties for the LV, RV, and a predefined infarcted region. The work of Rama and Skatulla [55] established a computationally efficient strategy to characterize mechanical properties of the heart wall and considered examples of a single ventricle (i.e., only LV) and bi-ventricle system, although all examples used artificially generated geometries (i.e., geometries were not derived directly from the segmentation of actual human imaging data).

One particular source of variation in previous studies on inverse characterization of heart wall properties is the use/processing of the measured data and type of objective function used in the optimization process. In some examples, the optimization process sought to match the measured cavity volume and/or pressure-volume relationship [29, 50, 55], which is a relatively small amount of data if trying to resolve a relatively large number of material parameters. Other studies have included objective functions based on matching the measured displacements and/or strains (and functions thereof) of the heart as it deforms [7, 45, 66, 28, 44, 6, 52, 46, 65]. However, measures of displacement or strain can be challenging to obtain, especially in a clinical setting, with current clinical imaging (through MR tagging or otherwise) not generally capable of detailed three-dimensional strain or displacement measurement. Alternatively, using more traditional imaging data (i.e., without tagging) may require a substantial pre-processing step to estimate strain or displacement from the imaging data, which could add computational expense and potentially be another source of error in the inverse solution estimation process. In contrast, a recent prior study by the authors [71] has presented a strategy to use the shape of the heart alone, without further preprocessing, as the target within the objective function of the inverse material property estimation procedure. Using *in silico* tests with simulated inverse characterization problems, the shape-based estimation procedure was shown to be capable of accurately estimating the magnitude of elastic material properties for a basic heart model as well as some amount of spacial variation in the properties. However, the approach was not previously tested on complete *in vivo* data for a heart, particularly as the prior study did not include a method to account for organ-level motion of the heart (i.e., rotation and translation) that would occur during the cardiac cycle.

This paper presents a novel clinically applicable approach to inversely estimate the *in vivo* mechanical material properties of the human heart, particularly the RV. This approach extends the prior work of the author on shape-based inverse characterization by including a strategy to account for the organ-level motion of the heart, and includes a method to evaluate the degree of heterogeneity of the material properties that can provide consistent estimates without the need for regularization. It should be noted that few of the previous studies have considered *in vivo* estimation of heterogeneous properties (i.e., only considered

a homogeneous heart wall) and even fewer considered more than 2 or 3 discrete regions of property variation. The capability of this inverse estimation approach is evaluated through the application to two clinically obtained datasets of standard cardiac MRI data and measured hemodynamics to estimate elastic material parameters throughout the left and right venrtricles. In particular, the ability to consistently identify elastic material parameters that agree with clinical expectations relating to the effect of PH on the human heart is shown. The following Section presents the overall inverse solution estimation algorithm. Then, Section 4.3 details the two clinical datasets used and shows and discusses the material property estimation results obtained from the inverse solution estimation algorithm. Lastly, conclusions and potential future directions are presented.

4.2 In Vivo Right Ventricle Inverse Material Characterization Algorithm

The overall inverse solution procedure utilized herein is based upon ongoing work of the authors to develop a shape-based strategy to inversely estimate mechanical properties of biological structures, particularly focused on the human heart [71]. In particular, the solution procedure follows the standard pattern of a PDE-constrained optimization method (i.e., model updating approach) for estimation of inverse problem solutions [8]. Figure 19 shows a flowchart of the overall inverse solution estimation procedure. The inputs to the algorithm are the cardiac images of the heart at end diastole and end systole and the associated intraventricular pressure within both ventricles at end diastole. The end systole images and intraventricular pressures are used to create a bi-ventricle model of the heart to estimate the patient specific, *in vivo*, passive (i.e., filling) ventricular behaviour, ending at end diastole (i.e., forward model). The end diastole images are used to estimate the shape of the right ventricle endocardial surface (RVES), which is the "target data" for the inverse solution estimation procedure. Provided with an initial guess for the material properties of the ventricular wall, iterative optimization is then applied. Within the optimization procedure, the difference between the target RVES shape and the RVES shape estimated by the bi-ventricle model is quantified and used to iteratively update the estimate of the material

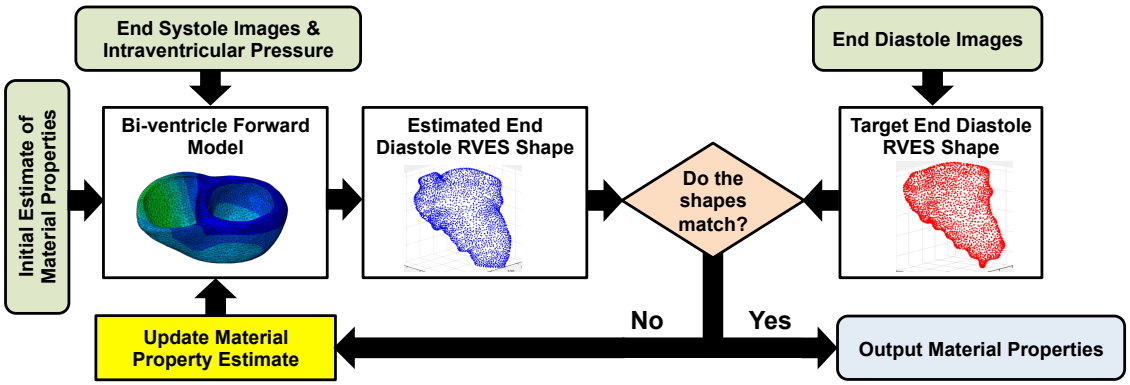

Figure 19: Flowchart of the overall optimization-based inverse solution estimation procedure.

properties until the solution converges or a termination criteria is reached. The remainder of this section provides further details of how each step was implemented in the current study, including the medical image processing, the forward problem to estimate the diastolic function, the objective function of the optimization procedure, and the proposed method of spatial parameterization of the material properties to be inversely estimated and the associated solution algorithm.

4.2.1 Image Processing

The proposed inverse estimation approach can be applied to any imaging modality, as long as three-dimensional representations of the right and left ventricle geometries can be estimated at phases in the cardiac cycle approximating the beginning of diastole (chosen as the end systole phase herein) and the end of diastole. The tissue volume of the left and right ventricles was extracted at end systole to be utilized by the forward modeling (detailed in the following section). However, as the present study is focused on characterizing the right ventricle due to the application of interest being pulmonary hypertension, only the right ventricle endocardial surface at end diastole was extracted to serve as the target shape in the inverse estimation procedure. Only the RV was considered since, as was noted in the introduction, the RV properties are the standard focus for evaluation of pulmonary

hypertension. Prior analyses by the authors [71] found that by targeting only the ventricle of interest, accurate properties can be obtained for that ventricle, while reducing sensitivity to the other portion that is considered unimportant. Another reason that the insensitivity to the left ventricle properties is important is that only the RV intraventricular pressure would normally be measured directly by cathetrarization for subjects with pulmonary hypertension, whereas the left ventricle intraventricular pressure would only be estimated from indirect measures (e.g., cuff measurement). Only the endocardial surface was used for the target shape, since this surface is normally more accurately estimated from imaging due to the blood boundary. Moreover, initial tests indicated there was little benefit to including the full ventricular wall thickness for estimating the desired properties, particularly as near incompressibility can normally be assumed.

For the work herein, both the end systolic bi-ventricle geometry and the end diastolic RVES were manually segmented and smoothed using the commercial image processing software Simpleware [1] under the supervision of a trained cardiologist. The segmentation included both ventricles from the apex to approximately the basal plane, and a standard recursive and discrete Gaussian filter was used to smooth all surfaces. A 4-node tetrahedral mesh was generated for the bi-ventricle geometry that was suitable for subsequent forward model numerical analysis, while a simple point cloud representation of the RVES was sufficient for the shape comparison in the optimization, as detailed in the following two Sections, respectively.

4.2.2 Forward Problem to Estimate Diastolic Function

The patient-specific bi-ventricle geometry extracted at end systole from the medical images was combined with the patient-specific intraventricular pressure at end diastole and implemented in a standard quasi-static nonlinear finite element analysis to estimate the diastolic function of the heart. In all cases, standard convergence tests were performed to ensure the mesh size was sufficiently small for accurate simulation. Although a bi-ventricle model is a considerable simplification of the cardiac geometry, as noted in the introduction, single-ventricle and bi-ventricle models have been commonly used in prior studies relating

[1] www.simpleware.com

to inverse characterization of properteries of the heart. In addition, using the end systolic geometry of the heart as the reference/unstressed state is a significant simplification, but is also consistent with similar studies and noted to be a beneficial choice to ensure consistency and solution identifiability [6]. An important note is that the methods proposed herein would not change in any way with a different forward model.

The support conditions included restricting the entire basal plane to have zero displacement in the transverse (i.e., axial) direction. In addition, the inner (i.e., endocardial) boundary of the basal plane of the left ventricle was arbitrarily chosen to have zero displacement in all directions to prevent rigid body motion, but to still allow flexibility, particularly for the RV as the key portion of interest. To simulate the passive diastolic process and estimate the end diastole RVES shape, the respective intraventricular pressures were applied uniformly to the left and right ventricles. Thus, it was assumed that capturing the blood flow was unnecessary to estimate the RVES shape at end diastole, which is again consistent with similar studies.

A quasi-incompressible transversely isotropic version of a Fung model shown in Guccione et al. [32] was chosen for the bi-ventricle constitutive behavior. There are many existing options for cardiac tissue constitutive models, and it should again be noted that the methods presented herein could be applied with any chosen forward model. The isochoric portion of the strain energy function for the chosen material model was defined as:

$$2\Psi(\mathbf{E}) = C_0 \left(e^{Q(\mathbf{E})} - 1\right) \tag{4.1}$$

with

$$Q(\mathbf{E}) = b_1 E_{ff}^2 + b_2(E_{cc}^2 + E_{rr}^2 + 2E_{cr}^2) + b_3(E_{fc}^2 + E_{fr}^2) \tag{4.2}$$

where $\mathbf{E}$ is the Green-Lagrange strain tensor with the indices f, c, and r referring to the fiber direction, cross-fiber in-plane direction, and radial direction, respectively, and C_0, b_1, b_2, and b_3 are the material parameters. In all analyses, the plane of isotropy was manually selected to coincide with the plane transverse to the thickness direction of the ventricular wall. To simplify the inverse problem and reduce the number of unknown material parameters, the relationship between nonlinearity parameters used in Genet et al. [29] was applied, such that $b_1 = B_0$, $b_2 = 0.4B_0$, and $b_3 = 0.7B_0$. Therefore, two parameters were needed to define the patient-specific material behaviour, the stiffness-related parameter, C_0, and the nonlinearity-related parameter, B_0. As such, the work herein was focused on the capability to inversely estimate the spatial variability of these two material parameters.

4.2.3 Shape-Based Objective Function

As noted previously, a major challenge/objective of the proposed inverse estimation approach was to be applicable to standard untagged medical imaging data, as would be obtained at present during evaluation of a disease such as pulmonary hypertension. Therefore, displacement and any derived quantify from displacement (e.g., strain) would not be directly available to target with the inverse estimation procedure. To account for this challenge without the need for additional processing steps to estimate displacement/deformation, the inverse solution procedure herein is based upon utilizing shape directly. The main component of this approach is the use of a modified version of the Hausdorff distance [21] to quantify

the difference between the target RVES shape and the shape of the RVES predicted by the forward problem with the current estimate of the material properties as:

$$H_d\left(S_i, S_j\right) = \max\left(M\left(S_i, S_j\right), M\left(S_j, S_i\right)\right) \tag{4.3}$$

with

$$M\left(S_i, S_j\right) = \frac{1}{N_i} \sum_{n=1}^{N_i} \min_{\vec{p}_m^j \in S_j} \left\| \vec{p}_n^i - \vec{p}_m^j \right\|, \tag{4.4}$$

where N_i is the total number of discrete points in the i^{th} shape, $\vec{p}_n^i$ is the vector of cartesian coordinates for the n^{th} point on the i^{th} shape, and $\| \cdot \|$ is the standard Euclidean distance operator. The Hausdorff distance was chosen, not only because of the relatively frequent use in shape comparison/matching applications, but also because of its intuitive nature and ease of implementation. The Hausdorff distance is a point-to-point matching (i.e., corresondence-based) method, with the modified version used here finding the average of the closest pairings between all the points on each shape.

A major component of this shape comparison approach that has not yet been addressed in prior work is that there would be an additional error if the Hausdorff distance metric was applied directly to compare the RVES at end diastole estimated by the forward model described with that extracted from the medical imaging. This additional error is due to the inability of the forward model to account for the organ-level (effectively rigid body) motion of the heart. To account for this discrepancy, standard iterative closest point (ICP) registration [16] was applied to estimate the rigid rotation and translation of the heart to match the RVES shape prior to applying the Hausdorff distance. This additional registration step allows the use of a substantially simplified representation of the heart (such as the bi-ventricle model described), while allowing the inverse solution procedure to focus primarily on the wall deformation, which is what the material parameters to be determined defines.

Combining the registration and the Hausdorff distance, the objective function to compare the estimated RVES shape, S_{sim}, with the target RVES shape, S_{target}, based on an estimated set of material parameters, $\vec{\gamma}$, could be written as:

$$J(\vec{\gamma}) = H_d\left(\left(R \times S_{\text{sim}}(\vec{\gamma}) + T\right), S_{\text{target}}\right), \tag{4.5}$$

where R and T are the ICP rotation and translation operators, respectively.

4.2.4 Parameterization of Material Properties and Solution Algorithm

The approach described to this point would be applicable to any constitutive model and parameterization of the associated material parameters. However, as noted, the work herein was particularly focused on the ability to consistently estimate spatial variations in the material properties of the ventricular wall. There are several different approaches that have been used to define the spatial distribution of material properties in similar applications, such as elastography [64]. These approaches generally vary depending on how much information can be assumed *a priori* about the distribution. For example, some studies have assumed that properties will only have localized variations and used a radial basis function description of the spatial distribution [4]. Alternatively, studies have often used very generalized mesh-based parameterization, where each element of a finite element-type mesh of the solid can have different values of material parameters [30]. Although generally applicable, these mesh-based approaches typically require some form of regularization that penalizes relatively large spatial variations in the parameters to obtain consistent and physically reasonable solutions.

To utilize a relatively generalized description of the spatial distribution without requiring additional regularization terms in the objective function, this study proposes an iterative approach to incrementally increase the spatial complexity of the material property distribution until the solution converges to a sufficiently accurate estimate of the heart behavior. In this approach, the optimization procedure is first applied assuming homogeneous properties and a randomly generated initial guess for the parameter values to inversely estimate the material

parameters that minimize the shape-based objective function. The geometry is then divided into multiple pieces and the optimization procedure is applied again, with the initial guess for the now multiple sets of parameters being the values estimated by the prior optimization assuming homogeneous properties. The procedure is repeated, each time increasing the number of regions allowed to have different material parameters and using the prior solution as the initial guess for a new optimization. The process ends when the estimated and target shapes sufficiently match, the solution no longer improves with increasing heterogeneity, or a maximum number of iterations is reached.

A final note is that any preferred optimization strategy can be used for each iteration to find the material parameters that minimize the shape-based objective function. Specifically, the interior point gradient-based optimization algorithm [14] with finite difference gradient approximation was applied to solve the optimization problem in the present study, with the specific solver parameters and stopping criteria provided in the example section. Algorithm 1 summarizes the entire inverse solution procedure to estimate the ventricular wall mechanical material properties.

4.3 Clinical Examples

Two anonymized patients that were clinically evaluated for potential heart disease were used as example cases to evaluate the capability to achieve consistent estimations of the ventricular wall mechanical material properties and validate the clinical applicability of the proposed inverse solution estimation approach. Cardiovascular magnetic resonance (CMR) images from two randomly chosen patients who underwent both CMR and right heart catheterization within a 2-day period were utilized. One patient was diagnosed with having pulmonary hypertension (i.e., a mean pulmonary arterial pressure greater than 25 $mmHg$), with a mean pulmonary arterial pressure of 49 $mmHg$, while the other patient was non-hypertensive with relatively normal heart function and a mean pulmonary arterial pressure of 23 $mmHg$. The RV ejection fraction of the non-hypertensive patient was in the range expected for normal function at approximately 50%, while the hypertensive patient had an

Algorithm 1 - *In vivo* ventricular wall material characterization algorithm.

Input: A bi-ventricle model of diastolic function (i.e., the forward model) and a target end diastolic RVES shape

Output: The ventricular wall material property distribution

Guess the initial material parameters for a homogeneous distribution of material properties
while the number of iterations is less than the maximum iterations **do**
    while the number of sub-iterations is less than the maximum sub-iterations **do**
        Simulate the forward model and extract the estimated RVES shape
        Register the estimated RVES shape to the target RVES shape
        Calculate the modified Hausdorff distance between the registered estimate and target RVES shapes
        if the optimization stopping criteria is met **then**
            break
        else
            Update the material parameters according to the chosen optimization procedure
        end if
    end while
    if the difference metric value or change in value between iterations is below the chosen tolerances **then**
        break
    else
        Divide the bi-ventricle geometry, increasing the number of spatial variations (i.e., parameters)
    end if
end while

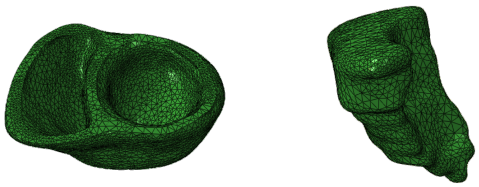

(a) (b)

Figure 20: (a) The volumetric mesh of the end systolic bi-ventricle geometry and (b) the surface mesh of the end diastolic right ventricle endocardial surface corresponding to the non-hypertensive patient.

ejection fraction of only 25%, indicating a significant deterioration in RV function for the hypertensive patient. It is important to note, however, that since the data used was acquired clinically, both patients were symptomatic, even though only one patient was diagnosed with pulmonary hypertension. Based on prior research examining the relationship between pulmonary hypertension and right heart mechanics [61], the right ventricle of the patient with pulmonary hypertension would be expected to have a higher stiffness than the right ventricle of the non-hypertensive patient.

4.3.1 Data Acquisition and Processing

Images were acquired for both patients using a 1.5-Tesla Siemens Magnetom Espree (Siemens Medical Solutions, Erlangen, Germany) equipped with a 32-channel cardiac coil. Standard breath-held cine imaging was acquired with steady-state free precession in the short axis orientation spanning the base to apex (6 mm slice thickness, 4 mm skip). Typical imaging parameters included 30 phases per R-R interval, matrix 256 by 144, flip angle 51°, TE 1.11 ms, and acceleration factor 3. Figures 20 and 21 show the bi-ventricle models at end systole and the target RVES at end diastole generated from the non-hypertensive and hypertensive patients' imaging data, respectively. As would be expected based on normal progression of pulmonary hypertension, the right ventricle of the hypertensive heart (seen

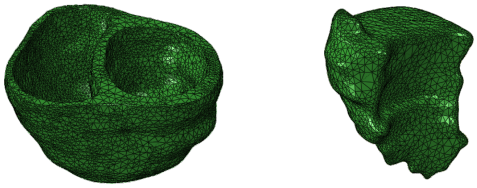

(a) (b)

Figure 21: (a) The volumetric mesh of the end systolic bi-ventricle geometry and (b) the surface mesh of the end diastolic right ventricle endocardial surface corresponding to the hypertensive patient.

on the left side of bi-ventricle models) is considerably larger and more "D"-shaped than the non-hypertensive heart, which maintains a crescent shaped and relatively small right ventricle.

The RV intraventricular pressures (as measured through catheterization) that were applied to simulate the diastolic process were 6 $mmHg$ and 26 $mmHg$ for the non-hypertensive and hypertensive patients, respectively, while the LV intraventricular pressures were arbitrarily set to a normal human value of 12 $mmHg$.

4.3.2 Optimization Procedure

As noted previously, a standard interior point gradient-based optimization procedure was applied to minimize the difference between the target RVES at end diastole extracted from the imaging data and that estimated by the bi-ventricle model. The stopping criteria for each minimization iteration was when the Euclidean norm of the change in parameter values was less than 10^{-25} or the number of iterations exceeded 50. In addition, Figure 22 shows how the heterogeneity of the bi-ventricle model was incrementally increased throughout the solution procedure, showing the hypertensive patient as a representative example. For both patients, following the initial homogeneous property estimation, the model was divided into three regions approximately corresponding to the RV free wall, the LV free wall, and the

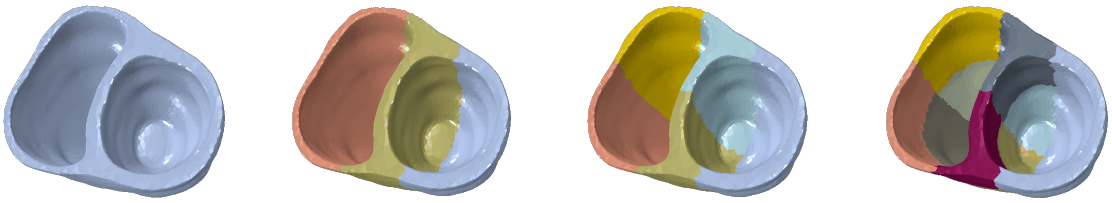

(a) (b) (c) (d)

Figure 22: The bi-ventricle geometry corresponding to the non-hypertensive patient showing (by colour change) the various divisions of the spatial distribution of the material properties evaluated, including (a) one division (i.e., homogeneous), (b) three divisions, (c) five divisions, and (d) nine divisions.

septum, with independent material parameters determined for each region. In subsequent steps only the RV and septum regions were further divided, keeping the LV as a simpler single region-case again based on the lack of importance and sensitivity of the LV properties. After analyzing the three-region case, the model was divided so that independent material parameters were estimated for the LV free wall and anterior and posterior portions of the RV free wall and septum (i.e., five regions). Lastly, the model was divided into nine regions corresponding to the LV free wall and upper and lower portions of the anterior and posterior portions of the RV free wall and septum, which was the point at which both patients were observed to converged with respect to the heterogeneity.

To obtain the initial homogeneous solutions, parameter values for the stiffness parameter (C_0) and the nonlinearity parameter (B_0) were randomly generated from uniform distributions within physiologically feasible ranges of $[0.6, 3]kPa$ and $[8, 30]$, respectively. The optimization process was repeated five times for the homogeneous solutions, with a new randomly generated initial guess each time to evaluate/ensure the solution consistency.

Table 9: Homogeneous material parameter values estimates for the non-hypertensive and hypertensive patients, as well as the associated modified Hausdorff distance (Objective Function) value following optimization.

	Non-Hypertensive		**Hypertensive**	
	$\mathbf{C_0}$ (kPa)	$\mathbf{B_0}$	$\mathbf{C_0}$ (kPa)	$\mathbf{B_0}$
Material Parameters	1.06	10.75	1.20	13.46
Objective Function (mm)	2.53		3.62	

4.3.3 Initial Homogeneous Solutions

Table 9 shows the "best" (i.e., lowest objective function value) parameter estimates for each patient from the five trials with randomly generated initial guesses and the corresponding Hausdorff distances. However, an important note is that all five of the randomly generated initial guesses for the material parameters resulted in approximately the same values for the final homogeneous estimate of the material parameters. To explore the consistency of the solution estimates further, Figure 23 shows the response surface (i.e., the value of the Hausdorff distance error metric) comparing the target end diastole surfaces to the estimated surfaces for values of the two material parameters within the given physiological bounds for the two patients. Both response surfaces could be considered smooth, with the surface corresponding to the hypertensive patient being less smooth than the non-hypertensive patient's surface. Both surfaces have troughs with values near to the minimum on the surfaces, which is due to the near non-uniqueness of the constitutive model parameters. However, for these examples, the minimum values on the surfaces were unique for both patients. More importantly, both response surfaces appear to be convex, which explains why the optimization process was able to consistently traverse the parameter space to identify nearly the same

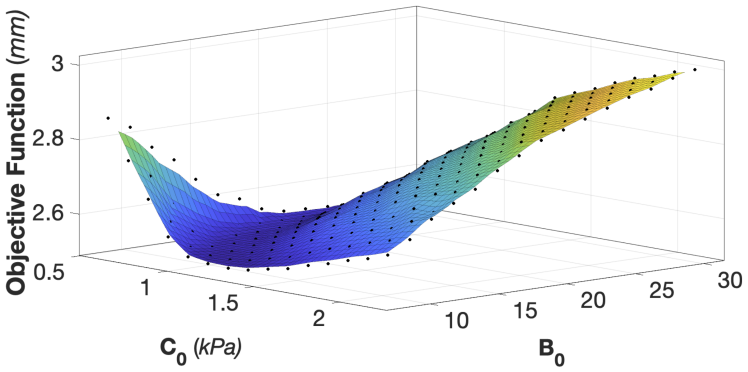

(a)

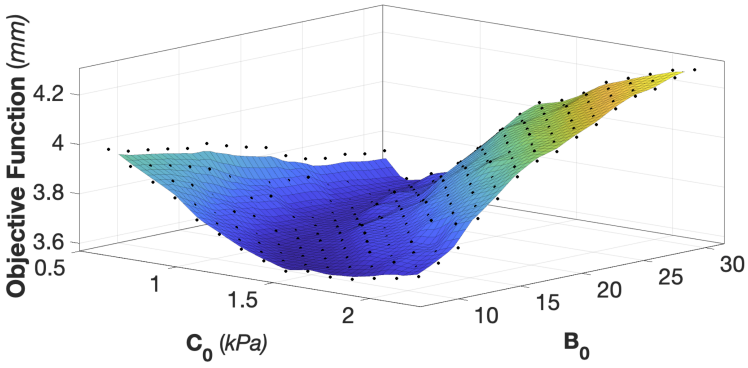

(b)

Figure 23: The modified Hausdorff distance (Objective Function) corresponding to a range of material parameter values for (a) the non-hypertensive and (b) hypertensive patients.

solutions each time. The consistency of the homogeneous estimate is particularly important as a consistent homogeneous estimate means that the entire algorithm will produce consistent estimates for the material parameters, even as the heterogeneity increases.

Again considering Table 9, the Hausdorff distances for the patients are both relatively small, with the results being that the average distance from any point on the target end diastole surfaces and the nearest points on the surfaces approximated with the final parameter estimates was approximately 2.5 mm for the non-hypertensive patient and 3.6 mm for the hypertensive patient. To provide context, a conservative estimate (i.e., lower bound) of the representative length of the internal volume of either RV is approximately 7 cm. Therefore, the maximum shape matching error is no more than 5% of a representative dimension. Thus, it can be inferred that even this simplest version of the substantially simplified cardiac model (in contrast to the actual human heart) could accurately estimate the shape change occurring for each patient during the diastolic process. However, the noticeably higher error for the hypertensive patient does indicate that there is likely additional model error for this patient. Unfortunately, it cannot be said whether this higher error for the hypertensive patient would be related to the material model, boundary conditions, or physical processes included (e.g., the neglected flow), but just that one or more of these deviations from the real system are more significant to the hypertensive patient than the non-hypertensive patient.

Comparing the parameter estimates for the two patients, both the stiffness parameter and the nonlinearity parameter are greater for the hypertensive patient than the non-hypertensive patient. To better understand the effect of these parameter differences, Figure 24 shows a plot of uniaxial stress versus uniaxial strain corresponding to the two parameter sets for strain values from 0 to 0.16, which was a larger strain magnitude than the maximum observed in the simulations. These material parameter results are consistent with the expectation that pulmonary hypertension leads to a heart wall (particularly the RV) with higher stiffness than a non-hypertensive heart, which instills further confidence in the results as they are consistent with physiological expectations.

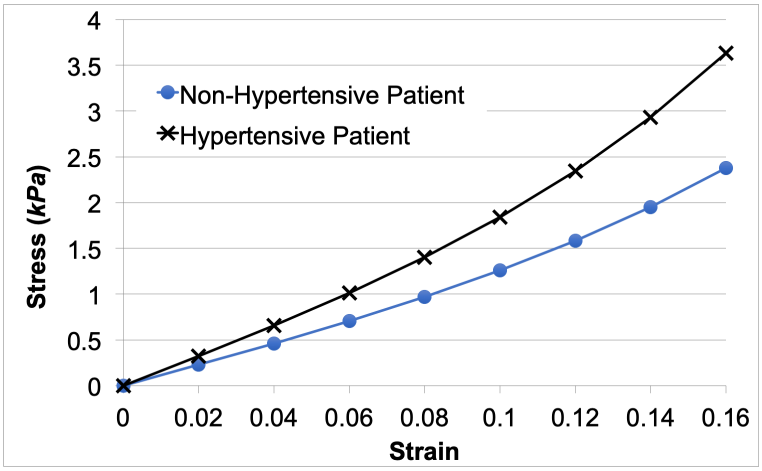

Figure 24: Uniaxial stress versus uniaxial strain corresponding to the inversely estimated homogeneous material parameters for the non-hypertensive and hypertensive patients.

4.3.4 Evaluation of Heterogeneity

As noted previously, the optimization procedure for both patients converged at nine divisions of the spatial distribution of material parameters. This means that the Hausdorff distances were not able to be further minimized for nine spatial divisions of properties, and the solutions with five spatial divisions of the properties were the final estimate for the inverse estimation algorithm. Tables 10 and 11 show the "best" parameter estimates for each spatial region for each patient and the corresponding Hausdorff distances for the iteration of the inverse solution estimation algorithm with three spatial divisions and five spatial divisions, respectively. As the algorithm increases the number of spatial divisions, the parameter values corresponding to each region significantly change while the corresponding Hausdorff distance error metric decreases, indicating that the algorithm was capable of traversing the solution space up until the point of convergence in terms of the number of spatial divisions. The amount of reduction in Hausdorff distance was relatively small, particularly in comparison to the magnitude of the parameter changes. However, the relatively small change in the error metric does not mean that the introduction of the heterogeneity was not important to accurately estimating the actual properties of the heart. The relative reduction in an error

Table 10: Parameter values estimates for the 3 spatial regions of the non-hypertensive and hypertensive patients corresponding to the left ventricle free wall (LVFW), the right ventricle free wall (RVFW), and the Septum, as well as the associated modified Hausdorff distance (Objective Function) value following optimization.

	Non-Hypertensive		**Hypertensive**	
	$\mathbf{C_0}$ (kPa)	$\mathbf{B_0}$	$\mathbf{C_0}$ (kPa)	$\mathbf{B_0}$
LVFW	1.47	13.83	1.50	14.56
RVFW	1.10	24.92	1.24	10.38
Septum	0.94	11.15	1.50	12.25
Objective Function (mm)	2.52		3.61	

metric for inverse problems such as this is not necessarily proportional to the increase in accuracy of the property estimate, and a small change in error may result in a substantial change in accuracy.

It is worth noting that a potential limitation of the algorithm employed is that it is certainly possible that a more accurate estimation could be obtained with a higher number of spatial divisions and/or a different form of spatial division. But, increasing the number of spatial divisions would likely lead to increasing non-uniqueness, would substantially increase the computational expense, and may do so for a relatively small and unnecessary increase in resolution. Yet, the critical point for the algorithm used is that since the homogeneous property estimates were consistent, then the final heterogeneous property estimates, including both the number of spatial divisions and the parameter values for each spatial region were consistent (i.e., a significantly different solution could not be produced using this algorithm) for both patients.

To examine the physical interpretation of the heterogeneous property results, the stress-strain relationships were again examined, with Figure 25 showing the uniaxial stress versus

Table 11: Parameter values estimates for the 5 spatial regions of the non-hypertensive and hypertensive patients corresponding to the left ventricle free wall (LVFW), the anterior (RVFW-A) and posterior (RVFW-P) portions of the right ventricle free wall, and the anterior (Septum-A) and posterior (Septum-P) portions of the septum, as well as the associated modified Hausdorff distance (Objective Function) value following optimization.

	Non-Hypertensive		**Hypertensive**	
	$\mathbf{C_0}$ (kPa)	$\mathbf{B_0}$	$\mathbf{C_0}$ (kPa)	$\mathbf{B_0}$
LVFW	1.48	12.42	1.49	18.01
RVFW-A	0.71	8.66	0.77	8.68
RVFW-P	1.50	24.36	1.49	13.26
Septum-A	0.69	8.68	1.50	13.89
Septum-P	0.66	8.92	0.69	9.76
Objective Function (mm)	2.36		3.23	

uniaxial strain corresponding to all five parameter sets for each of the two patients, again for strain values from 0 to 0.16. Although properties of the LV are shown and there is a clear difference between the patients, recall that the LV properties were intentionally insensitive in the inverse problem, and so should not be considered significant. Instead, focusing on the RV free wall and septum properties, one immediate observation is that the stiffness of the RV posterior free wall of the non-hypertensive patient appears to be far greater than any other component of either patient. However, this may not mean that the material properties of the non-hypertensive patient's RV posterior free wall are actually stiffer than the rest of the heart. Particularly since the material model used was nonlinear, the parameter increase may simply indicate that the associated portion of the heart deforms less than the others.

To examine the deformation of both hearts predicted by the bi-ventricle models with the estimated material parameters, Figure 26 shows the distribution of the maximum principal strain of each heart at end diastole. Overall, the non-hypertensive patient's heart deforms considerably more than the hypertensive patient's heart, which is expected based on the considerably lower RV ejection fraction corresponding to the hypertensive patient. However, the deformation (i.e., strain) of the non-hypertensive patient's heart is also considerably more non-uniform, and the RV posterior free wall of the non-hypertensive patient deforms approximately an order of magnitude less than the rest of the heart. One possibility for this regional difference in deformation could be additional stiffness in the real system that is provided by the valve in that region of the heart or other connective tissues that are not accounted for in the bi-ventricle model, or simply error due to the simplified boundary conditions used to support the bi-ventricle model in general. This difference in amount of deformation is important, as it emphasizes a major limitation in all types of *in vivo* material characterization. The characterization algorithm is limited by the excitation that happens naturally *in vivo*. Since one portion of the heart is not excited substantially for the estimation herein, then the estimation of the corresponding parameters/properties should not be relied upon as a predictive measure of the actual wall properties in the same way as can be for the other regions that experience more deformation. Thus, comparing the regions of the two heart walls (non-hypertensive and hypertensive) that experience relatively large deformation, the properties of the hypertensive patient's heart are considerably more non-uniform,

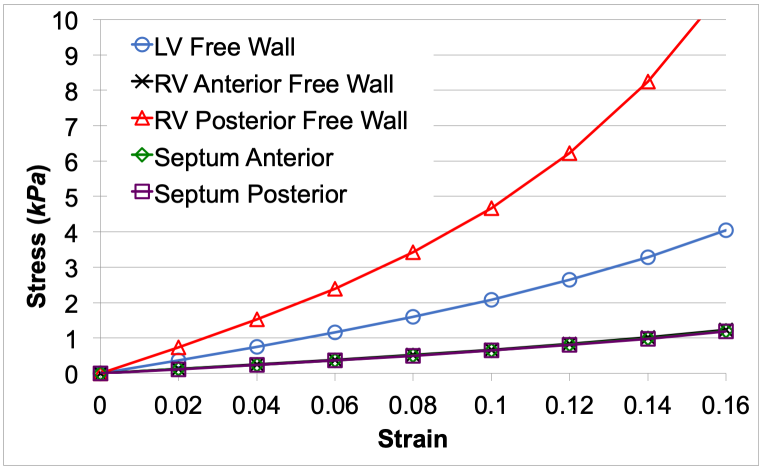

(a)

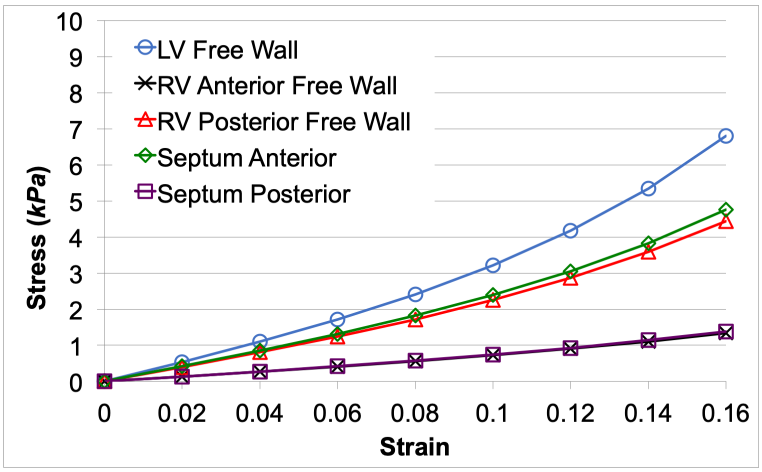

(b)

Figure 25: Uniaxial stress versus uniaxial strain corresponding to the inversely estimated material parameters for the five divisions of the heart wall approximating the LV free wall, anterior and posterior portions of the RV free wall, and anterior and posterior portions of the septum for the (a) non-hypertensive patient and (b) hypertensive patient.

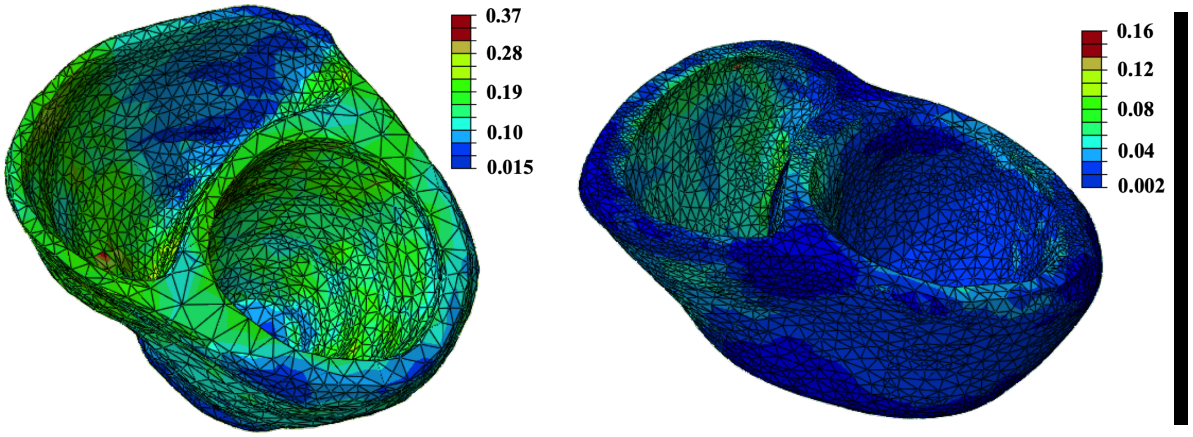

(a) (b)

Figure 26: Distribution of the maximum principal strain at end diastole for the bi-ventricle models with the final estimates of the material parameters for the (a) non-hypertensive patient and (b) hypertensive patient.

especially considering the relative uniformity of the deformation of the hypertensive heart. While the properties of two portions of the hypertensive patient's heart, the anterior of the RV free wall and the posterior of the septum, were relatively similar to the properties of the non-hypertensive patient's heart, the properties of the other two regions were nearly doubled (i.e., the stiffness was approximately doubled). As for the previous homogeneous property estimate, the relatively higher stiffness of the hypertensive patient's heart is consistent with clinical expectations. However, the relative non-uniformity of the material property estimate for the hypertensive patient's heart and the specific regions that were more stiff than others was not necessarily expected. Substantial work remains to test and potentially develop the *in vivo* material characterization algorithm further, particularly to investigate patient sets of substantive size. Yet, such revelations relating to heterogeneity are exactly what this inverse material characterization algorithm is intended for, as the identification of regional variations in the heart wall properties may help to discriminate between hearts that are adapting well or poorly to pressure overloads, along with when and how intervention can be most effective.

4.4 Conclusions

A strategy has been presented to extend a shape-based inverse material characterization algorithm to be used for estimation of the *in vivo* mechanical material properties of the heart from standard clinical imaging and hemodynamic measurements. A key component of the inverse estimation algorithm is the use of the shape-based objective function in combination with a rigid registration process that allows for the use of basic (e.g., untagged) medical imaging data in combination with significantly simplified forward model representations of the heart mechanical function, while still accounting for the organ-level rotation and translation. The proposed approach also incorporated a strategy to incrementally increase the degree of heterogeneity to estimate relatively arbitrary spatial variability of material properties without the need for regularization. Prior work using simulated inverse problems has shown that the shape-based objective function could be used within an optimization-based inverse solution estimation procedure to accurately estimate mechanical material parameters. Therefore, the present study was focused on the application to real clinically obtained input and target data for the inverse problem, to evaluate the real-life applicability, particularly in terms of the potential to obtain consistent and physically meaningful solutions. As such, the proposed approach was applied to two clinically obtained datasets corresponding to a patient with relatively normal cardiac function and a patient with severe pulmonary hypertension, and patient-specific pressure-driven bi-ventricle models were used to estimate diastolic function for the corresponding forward problems. In both cases, a solution estimate for the distribution of mechanical material properties throughout the bi-ventricle model was obtained that resulted in an accurate match between the end diastolic shape extracted from the medical imaging data and that approximated by the bi-ventricle model. Moreover, the inverse solutions estimates were both nearly unique, largely due to the procedure to incrementally increase heterogeneity and the observation that the initial homogeneous property estimates were nearly unique regardless of the starting point of the optimization. The inverse solution estimates were also consistent with the physical expectation that the heart corresponding to the patient with pulmonary hypertension would be stiffer overall, even though less deformation occurs during the diastolic filling. An impor-

tant observation was that the spatial variation of properties in both hearts was estimated to be significant, which is at odds with the assumption made in many similar studies on inverse methods that the properties of the heart wall are homogeneous or have relatively limited spatial variability. However, one concern that requires further exploration is that the uncontrolled nature of the excitation means that some portions of the heart wall contribute more to the mechanical function than others, and there is substantially more confidence in the accuracy in estimating the properties of these regions. Other areas of potential future work include incorporating more complete/realistic forward models, particularly to improve the realism of boundary conditions and to more realistically represent the cardiac cycle, as well as improving the generalization of the material property representation while maintaining or improving computational efficiency.

5.0 Current Capabilities and Future Direction

For the first portion of the work herein, a statistical shape analysis framework was utilized to evaluate a unique clinically obtained dataset of patients with and without pulmonary hypertension (PH). The dataset contained 50 total patients (33 of which had PH) and the shape analysis was applied to the shapes of the right ventricle endocardial surface (RVES) of each patient at end diastole and end systole to extract a set of shape features that are most significant to the dataset of 100 shapes (i.e., describe the features that most vary). The framework was able to derive shape features of the RVES that have clear correlation to the state of PH, as seen through quantifying the correlation between modal coefficients (i.e., magnitude of shape features) for each patient and the clinical measures used to diagnose PH, such as pulmonary arterial pressure. These significant shape features were also noted to have specific and clear physical appearances that corresponded to observations made historically in clinical settings. Two shape features in particular stood out, one shape feature that appeared to describe the thickening of the overall RVES and one that appeared to describe the flattening of the septum, both of which have been previously noted qualitatively to be linked to the state of PH. Therefore, these shape features may provide a uniquely quantitative measure to evaluate the presence of PH entirely noninvasively (i.e., only using imaging and no invasive hemodynamic measures). More importantly, the shape feature relating to the flattening of the septum was shown to be significantly correlated with the outcome of the patient, defined by hospitalization with heart failure and/or death. The shape modal coefficient was seen to be substantially more related to the patient outcome than the measures used to diagnose PH themselves. Overall, the results of the shape analysis provide strong evidence that shape of the right ventricle can be used to predict both the state of PH and the likelihood of adverse outcomes for patients with PH, such as death, and justify further investigation.

Specific future directions for statistical shape analysis should include efforts to automate or at least semi-automate the shape analysis procedure, as the current process is both time consuming and includes several manual steps that can reduce analysis consistency. This effort

to automate should simultaneously explore the robustness of the shape analysis, seeking to identify the analysis choices that maximize not just the ability of the results to predict patient health, but also the consistency of these results regardless of operator, data source, etc. Once sufficiently automated and robust, this approach should be applied to a large-scale dataset to solidify a clinically applicable diagnostic and prognostic tool to aid decision making in the treatment of PH.

The second portion of the work herein focused on the development of a new strategy to estimate the mechanical material properties of the heart wall, particularly the right ventricle (RV), towards establishing an alternate measure of RV mechanical function to potentially complement the shape analysis approach. More specifically, an optimization-based inverse solution estimation algorithm was developed to estimate the heart wall mechanical material parameters (e.g., stiffness and nonlinearity parameters) using standard (i.e., untagged) medical imaging data and known internal pressure as excitation. A key component of this inverse solution estimation approach was the use of a shape-based objective function to compare the numerically simulated estimate of the heart function to the shape of the heart extracted from the medical images. By using shape, the approach is a more direct use of available data and avoids the need for time consuming and potentially error-adding pre-processing to estimate the displacement or deformation of the heart wall from the imaging data. First, the algorithm was evaluated through *in silico* testing (i.e., simulated inverse problems) using a bi-ventricle (i.e., left and right ventricle combined) finite element model derived from medical imaging data. The bi-ventricle model was given known heterogeneous material properties and known internal pressures were applied to simulate the inverse problem target shape. Then, the inverse solution estimation approach was applied to estimate the material properties as though they were unknown. These *in silico* tests showed that accurate estimations of mechanical material parameters can be obtained targeting only the shape of the deformed structure, even in the presence of significant model error. Additionally, it was shown that accuracy of a specific portion of the structure (e.g., the RV) could be increased while simultaneously reducing the sensitivity to other unimportant portions of the structure (e.g., the left ventricle) by only including the shape of the desired portion in the objective function. Lastly, the inverse solution estimation algorithm was extended to be fully applicable to real

clinically obtained patient data. In particular, a rigid registration component was incorporated so that simplified representations of the heart function, such as the bi-ventricle model used herein, could be used as the forward model in the solution procedure and still account for the organ-level motion of the heart. In addition, an approach to estimate generalized heterogeneity of the material properties was implemented that incrementally increases the degree of heterogeneity of the material properties. This final version of the inverse solution estimation algorithm was applied to estimate the mechanical material properties of the right and left ventricles of two patients, one with normal heart function and one with severe PH, using only standard clinical imaging data and measured intraventricular pressures. The inverse estimation algorithm was shown to provide highly consistent estimates of the material properties, largely due to the consistency of the initial step of estimating homogeneous properties. The results were consistent with clinical expectation that the patient with PH would have an overall stiffer RV, providing some validation of the inverse solution estimation algorithm. Moreover, the estimated material property distributions for both patients predicted a significant degree of heterogeneity, highlighting the importance of considering spatial variation in mechanical material properties when evaluating the heart.

Although the initial proof-of-concept level results herein are promising, significant work remains to advance this inverse solution estimation algorithm. In addition to examining more test cases and incorporating more realistic material properties and boundary conditions into the forward model, several aspects of the solution procedure should be explored further. In particular, examination of alternate shape-based objective functionals will be important to identify an approach that balances solution accuracy, consistency, and computational efficiency. Similarly to the statistical shape analysis work, it will also be important to improve automation of the procedure to ensure solution consistency and reduce the time cost to the user for this type of approach to translate into clincal practice.

Bibliography

[1] Christiane M Abouzeid, Tara Shah, Ansh Johri, Jonathan W Weinsaft, and Jiwon Kim. Multimodality imaging of the right ventricle. *Current treatment options in cardiovascular medicine*, 19(11):82, 2017.

[2] Karima Addetia, Francesco Maffessanti, Megan Yamat, Lynn Weinert, Akhil Narang, Benjamin H. Freed, Victor Mor-Avi, and Roberto M. Lang. Three-dimensional echocardiography-based analysis of right ventricular shape in pulmonary arterial hypertension. *European Heart Journal – Cardiovascular Imaging*, 17(5):564–575, jul 2015.

[3] Jean-Sébastien Affagard, Pierre Feissel, and Sabine F Bensamoun. Identification of hyperelastic properties of passive thigh muscle under compression with an inverse method from a displacement field measurement. *Journal of biomechanics*, 48(15):4081–4086, 2015.

[4] M. A. Aguilo, W. Aquino, J. C. Brigham, and M. Fatemi. An inverse problem approach for elasticity imaging through vibroacoustics. *IEEE Transactions on Medical Imaging*, 29(4):1012–1021, 2010.

[5] Brage H Amundsen, Thomas Helle-Valle, Thor Edvardsen, Hans Torp, Jonas Crosby, Erik Lyseggen, Asbjørn Støylen, Halfdan Ihlen, João AC Lima, Otto A Smiseth, et al. Noninvasive myocardial strain measurement by speckle tracking echocardiography: validation against sonomicrometry and tagged magnetic resonance imaging. *Journal of the American College of Cardiology*, 47(4):789–793, 2006.

[6] Liya Asner, Myrianthi Hadjicharalambous, Radomir Chabiniok, Devis Peresutti, Eva Sammut, James Wong, Gerald Carr-White, Philip Chowienczyk, Jack Lee, Andrew King, et al. Estimation of passive and active properties in the human heart using 3d tagged mri. *Biomechanics and modeling in mechanobiology*, 15(5):1121–1139, 2016.

[7] Kevin F Augenstein, Brett R Cowan, Ian J LeGrice, and Alistair A Young. Estimation of cardiac hyperelastic material properties from mri tissue tagging and diffusion tensor imaging. In *International Conference on Medical Image Computing and Computer-Assisted Intervention*, pages 628–635. Springer, 2006.

[8] Stéphane Avril. Hyperelasticity of soft tissues and related inverse problems. In *Material Parameter Identification and Inverse Problems in Soft Tissue Biomechanics*, pages 37–66. Springer, 2017.

[9] Per Bergstrom and Ove Edlund. Robust registration of point sets using iteratively reweighted least squares. *Computational Optimization and Applications*, 58(3):543–561, feb 2014.

[10] Per Bergstrom and Ove Edlund. Robust registration of surfaces using a refined iterative closest point algorithm with a trust region approach. *Numerical Algorithms*, 74(3):755–779, jul 2016.

[11] Norman F Boyd, Qing Li, Olga Melnichouk, Ella Huszti, Lisa J Martin, Anoma Gunasekara, Gord Mawdsley, Martin J Yaffe, and Salomon Minkin. Evidence that breast tissue stiffness is associated with risk of breast cancer. *PloS one*, 9(7), 2014.

[12] G. Boyer, J. Molimard, M. Ben Tkaya, H. Zahouani, M. Pericoi, and S. Avril. Assessment of the in-plane biomechanical properties of human skin using a finite element model updating approach combined with an optical full-field measurement on a new tensile device. *Journal of the Mechanical Behavior of Biomedical Materials*, 27:273 – 282, 2013.

[13] John C Brigham and Wilkins Aquino. Inverse viscoelastic material characterization using pod reduced-order modeling in acoustic–structure interaction. *Computer Methods in Applied Mechanics and Engineering*, 198(9-12):893–903, 2009.

[14] Richard H. Byrd, Mary E. Hribar, and Jorge. Nocedal. An interior point algorithm for large-scale nonlinear programming. *SIAM Journal on Optimization*, 9(4):877–900, 1999.

[15] Chen-Ket Chai, Ali C. Akyildiz, Lambert Speelman, Frank J.H. Gijsen, Cees W.J. Oomens, Marc R.H.M. van Sambeek, Aad van der Lugt, and Frank P.T. Baaijens. Local axial compressive mechanical properties of human carotid atherosclerotic plaques - characterisation by indentation test and inverse finite element analysis. *Journal of Biomechanics*, 46(10):1759 – 1766, 2013.

[16] Dmitry Chetverikov, Dmitry Stepanov, and Pavel Krsek. Robust euclidean alignment of 3d point sets: the trimmed iterative closest point algorithm. *Image and vision computing*, 23(3):299–309, 2005.

[17] Kelly M Chin, Nick HS Kim, and Lewis J Rubin. The right ventricle in pulmonary hypertension. *Coronary artery disease*, 16(1):13–18, 2005.

[18] Mayo Clinic. Pulmonary hypertension symptoms, 2020.

[19] Yaghoub Dabiri, Kevin L Sack, Nuno Rebelo, Peter Wang, Yunjie Wang, Jenny S Choy, Ghassan S Kassab, and Julius M Guccione. Method for calibration of left ventricle material properties using three-dimensional echocardiography endocardial strains. *Journal of biomechanical engineering*, 141(9), 2019.

[20] Timothy JW Dawes, Antonio de Marvao, Wenzhe Shi, Tristan Fletcher, Geoffrey MJ Watson, John Wharton, Christopher J Rhodes, Luke SGE Howard, J Simon R Gibbs, Daniel Rueckert, et al. Machine learning of three-dimensional right ventricular motion enables outcome prediction in pulmonary hypertension: a cardiac mr imaging study. *Radiology*, 283(2):381–390, 2017.

[21] M-P Dubuisson and Anil K Jain. A modified hausdorff distance for object matching. In *Proceedings of 12th international conference on pattern recognition*, volume 1, pages 566–568. IEEE, 1994.

[22] Longling Fan, Jing Yao, Chun Yang, Zheyang Wu, Di Xu, and Dalin Tang. Material stiffness parameters as potential predictors of presence of left ventricle myocardial infarction: 3d echo-based computational modeling study. *Biomedical engineering online*, 15(1):34, 2016.

[23] L. Fernandez-Friera, A. Garcia-Alvarez, G. Guzman, F. Bagheriannejad-Esfahani, W. Malick, A. Nair, V. Fuster, M. J. Garcia, and J. Sanz. Apical right ventricular dysfunction in patients with pulmonary hypertension demonstrated with magnetic resonance. *Heart*, 97(15):1250–1256, jun 2011.

[24] Office for National Statistics. Deaths by single year of age tables, uk, 2020.

[25] Alexandre Franquet, Stéphane Avril, Rodolphe Le Riche, and Pierre Badel. Identification of heterogeneous elastic properties in stenosed arteries: a numerical plane strain study. *Computer Methods in Biomechanics and Biomedical Engineering*, 15(1):49–58, 2012.

[26] Adaani Frost, David Badesch, J. Simon R. Gibbs, Deepa Gopalan, Dinesh Khanna, Alessandra Manes, Ronald Oudiz, Toru Satoh, Fernando Torres, and Adam Torbicki. Diagnosis of pulmonary hypertension. *European Respiratory Journal*, 53(1), 2019.

[27] Nazzareno Galiè, Marc Humbert, Jean-Luc Vachiery, Simon Gibbs, Irene Lang, Adam Torbicki, Gérald Simonneau, Andrew Peacock, Anton Vonk Noordegraaf, Maurice Beghetti, et al. 2015 esc/ers guidelines for the diagnosis and treatment of pulmonary hypertension: the joint task force for the diagnosis and treatment of pulmonary hypertension of the european society of cardiology (esc) and the european respiratory society (ers) endorsed by: Association for european paediatric and congenital cardiology (aepc), international society for heart and lung transplantation (ishlt). *European Respiratory Journal*, 46(4):903–975, 2015.

[28] H Gao, WG Li, L Cai, C Berry, and XY Luo. Parameter estimation in a holzapfel–ogden law for healthy myocardium. *Journal of engineering mathematics*, 95(1):231–248, 2015.

[29] Martin Genet, Lik Chuan Lee, Rebecca Nguyen, Henrik Haraldsson, Gabriel Acevedo-Bolton, Zhihong Zhang, Liang Ge, Karen Ordovas, Sebastian Kozerke, and Julius M. Guccione. Distribution of normal human left ventricular myofiber stress at end diastole and end systole: a target for in silico design of heart failure treatments. *Journal of Applied Physiology*, 117(2):142–152, 2014. PMID: 24876359.

[30] Nachiket H Gokhale, Paul E Barbone, and Assad A Oberai. Solution of the nonlinear elasticity imaging inverse problem: the compressible case. *Inverse Problems*, 24(4):045010, jun 2008.

[31] Ekkehard Grünig and Andrew J. Peacock. Imaging the heart in pulmonary hypertension: an update. *European Respiratory Review*, 24(138):653–664, nov 2015.

[32] Julius M Guccione, Andrew D McCulloch, and LK Waldman. Passive material properties of intact ventricular myocardium determined from a cylindrical model. 1991.

[33] Myrianthi Hadjicharalambous, Liya Asner, Radomir Chabiniok, Eva Sammut, James Wong, Devis Peressutti, Eric Kerfoot, Andrew King, Jack Lee, Reza Razavi, et al. Non-invasive model-based assessment of passive left-ventricular myocardial stiffness in healthy subjects and in patients with non-ischemic dilated cardiomyopathy. *Annals of biomedical engineering*, 45(3):605–618, 2017.

[34] Michael R Hill, Marc A Simon, Daniela Valdez-Jasso, Will Zhang, Hunter C Champion, and Michael S Sacks. Structural and mechanical adaptations of right ventricle free wall myocardium to pressure overload. *Annals of biomedical engineering*, 42(12):2451–2465, 2014.

[35] Marc Humbert, Olivier Sitbon, Ari Chaouat, Michèle Bertocchi, Gilbert Habib, Virginie Gressin, Azzedine Yaïci, Emmanuel Weitzenblum, Jean-François Cordier, François Chabot, et al. Clinical perspective. *Circulation*, 122(2):156–163, 2010.

[36] Andreas P. Kalogeropoulos, J. David Vega, Andrew L. Smith, and Vasiliki V. Georgiopoulou. Pulmonary hypertension and right ventricular function in advanced heart failure. *Congestive Heart Failure*, 17(4):189–198, jul 2011.

[37] Jens Klein, Joyce McLaughlin, and Daniel Renzi. Improving arrival time identification in transient elastography. *Physics in Medicine and Biology*, 57:2151–2168, 2012.

[38] Peter J Leary, Christopher E Kurtz, Catherine L Hough, Mary-Pierre Waiss, David D Ralph, and Florence H Sheehan. Three-dimensional analysis of right ventricular shape and function in pulmonary hypertension. *Pulmonary circulation*, 2(1):34–40, 2012.

[39] Y. Liu, G. Wang, and L. Z. Sun. Elastography method to identify material distribution in two-phase nonlinear media. *Journal of Engineering Mechanics*, 140(5):04014010, 2014.

[40] Kenneth Mangion, Hao Gao, Dirk Husmeier, Xiaoyu Luo, and Colin Berry. Advances in computational modelling for personalised medicine after myocardial infarction. *Heart*, 104(7):550–557, 2018.

[41] Charlène Mauger, Kathleen Gilbert, Aaron M Lee, Mihir M Sanghvi, Nay Aung, Kenneth Fung, Valentina Carapella, Stefan K Piechnik, Stefan Neubauer, Steffen E Petersen, et al. Right ventricular shape and function: cardiovascular magnetic resonance reference morphology and biventricular risk factor morphometrics in uk biobank. *Journal of Cardiovascular Magnetic Resonance*, 21(1):41, 2019.

[42] Gert-Jan Mauritz, Taco Kind, J Tim Marcus, Harm-Jan Bogaard, Mariëlle van de Veerdonk, Pieter E Postmus, Anco Boonstra, Nico Westerhof, and Anton Vonk-Noordegraaf. Progressive changes in right ventricular geometric shortening and long-term survival in pulmonary arterial hypertension. *Chest*, 141(4):935–943, 2012.

[43] Gert-Jan Mauritz, Anton Vonk-Noordegraaf, Taco Kind, Sulaiman Surie, Jaap J Kloek, Paul Bresser, Nabil Saouti, Joachim Bosboom, Nico Westerhof, and J Tim Marcus. Pulmonary endarterectomy normalizes interventricular dyssynchrony and right ventricular systolic wall stress. *Journal of Cardiovascular Magnetic Resonance*, 14(1):5, 2012.

[44] Dimitri Mojsejenko, Jeremy R McGarvey, Shauna M Dorsey, Joseph H Gorman, Jason A Burdick, James J Pilla, Robert C Gorman, and Jonathan F Wenk. Estimating passive mechanical properties in a myocardial infarction using mri and finite element simulations. *Biomechanics and modeling in mechanobiology*, 14(3):633–647, 2015.

[45] Arun U. Nair, David G. Taggart, and Frederick J. Vetter. Optimizing cardiac material parameters with a genetic algorithm. *Journal of Biomechanics*, 40(7):1646 – 1650, 2007.

[46] Anastasia Nasopoulou, Anoop Shetty, Jack Lee, David Nordsletten, C Aldo Rinaldi, Pablo Lamata, and Steven Niederer. Improved identifiability of myocardial material parameters by an energy-based cost function. *Biomechanics and modeling in mechanobiology*, 16(3):971–988, 2017.

[47] Shayan Shaghayeq Nazari and Pinku Mukherjee. An overview of mammographic density and its association with breast cancer. *Breast cancer*, 25(3):259–267, 2018.

[48] Ivan Nenadic, Lance Mynderse, Douglas Husmann, Mohammad Mehrmohammadi, Mahdi Bayat, Aparna Singh, Max Denis, Matthew W Urban, Azra Alizad, and Mostafa Fatemi. Noninvasive evaluation of bladder wall mechanical properties as a function of filling volume: Potential application in bladder compliance assessment. *PLoS One*, 11(6), 6 2016.

[49] Assad A Oberai, Nachiket H Gokhale, and Gonzalo R Feij o. Solution of inverse problems in elasticity imaging using the adjoint method. *Inverse Problems*, 19(2):297–313, feb 2003.

[50] Arnab Palit, Sunil K. Bhudia, Theodoros N. Arvanitis, Glen A. Turley, and Mark A. Williams. In vivo estimation of passive biomechanical properties of human myocardium. *Medical & Biological Engineering & Computing*, 56(9):1615–1631, 2018.

[51] Arnab Palit, Pasquale Franciosa, Sunil K Bhudia, Theodoros N Arvanitis, Glen A Turley, and Mark A Williams. Passive diastolic modelling of human ventricles: Effects of base movement and geometrical heterogeneity. *Journal of biomechanics*, 52:95–105, 2017.

[52] Luigi E Perotti, Aditya V S Ponnaluri, Shankarjee Krishnamoorthi, Daniel Balzani, Daniel B Ennis, and William S Klug. Method for the unique identification of hyperelastic material properties using full-field measures. application to the passive myocardium material response. *International journal for numerical methods in biomedical engineering*, 33(11):10.1002/cnm.2866, 11 2017.

[53] Gianmarco F Pinton, Jeremy J Dahl, and Gregg E Trahey. Rapid tracking of small displacements with ultrasound. *IEEE transactions on ultrasonics, ferroelectrics, and frequency control*, 53(6):1103–1117, 2006.

[54] Katarzyna Ptaszyńska-Kopczyńska, Anna Krentowska, Emilia Sawicka, Anna Skoneczny, Małgorzata Jasiewicz, Małgorzata Knapp, Włodzimierz J. Musiał, Bożena Sobkowicz, and Karol A. Kamiński. The strengths and weaknesses of non-invasive parameters obtained by echocardiography and cardiopulmonary exercise testing in comparison with the hemodynamic assessment by the right heart catheterization in patients with pulmonary hypertension. *Advances in Medical Sciences*, 62(1):39–44, mar 2017.

[55] Ritesh Rao Rama and Sebastian Skatulla. Real-time nonlinear solid mechanics computations for fast inverse material parameter optimization in cardiac mechanics. *Journal of Engineering Mechanics*, 145(4):04019020, 2019.

[56] Anne M Robertson, Xinjie Duan, Khaled M Aziz, Michael R Hill, Simon C Watkins, and Juan R Cebral. Diversity in the strength and structure of unruptured cerebral aneurysms. *Annals of biomedical engineering*, 43(7):1502–1515, 2015.

[57] Chao Sang, Spandan Maiti, Ronald N Fortunato, Julia Kofler, and Anne M Robertson. A uniaxial testing approach for consistent failure in vascular tissues. *Journal of biomechanical engineering*, 140(6), 2018.

[58] Partho P Sengupta, Vijay K Krishnamoorthy, Josef Korinek, Jagat Narula, Mani A Vannan, Steven J Lester, Jamil A Tajik, James B Seward, Bijoy K Khandheria, and Marek Belohlavek. Left ventricular form and function revisited: applied translational science to cardiovascular ultrasound imaging. *Journal of the American Society of Echocardiography*, 20(5):539–551, 2007.

[59] Marc A Simon, Christopher Deible, Michael A Mathier, Joan Lacomis, Orly Goitein, Sanjeev G Shroff, and Michael R Pinsky. Phenotyping the right ventricle in patients with pulmonary hypertension. *Clinical and translational science*, 2(4):294–299, 2009.

[60] Gérald Simonneau, Ivan M Robbins, Maurice Beghetti, Richard N Channick, Marion Delcroix, Christopher P Denton, C Gregory Elliott, Sean P Gaine, Mark T Gladwin, Zhi-Cheng Jing, et al. Updated clinical classification of pulmonary hypertension. *Journal of the American College of Cardiology*, 54(1 Supplement):S43–S54, 2009.

[61] Pia Trip, Silvia Rain, M Louis Handoko, Cathelijne Van der Bruggen, Harm J Bogaard, J Tim Marcus, Anco Boonstra, Nico Westerhof, Anton Vonk-Noordegraaf,

and S Frances. Clinical relevance of right ventricular diastolic stiffness in pulmonary hypertension. *European Respiratory Journal*, 45(6):1603–1612, 2015.

[62] Mariëlle C van de Veerdonk, Harm J Bogaard, and Norbert F Voelkel. The right ventricle and pulmonary hypertension. *Heart failure reviews*, 21(3):259–271, 2016.

[63] Anton Vonk-Noordegraaf, François Haddad, Kelly M Chin, Paul R Forfia, Steven M Kawut, Joost Lumens, Robert Naeije, John Newman, Ronald J Oudiz, Steve Provencher, et al. Right heart adaptation to pulmonary arterial hypertension: physiology and pathobiology. *Journal of the American College of Cardiology*, 62(25 Supplement):D22–D33, 2013.

[64] Mengyu Wang and John C Brigham. A generalized computationally efficient inverse characterization approach combining direct inversion solution initialization with gradient-based optimization. *Computational Mechanics*, 59(3):507–521, 2017.

[65] Zhinuo J. Wang, Vicky Y. Wang, Thiranja P. Babarenda Gamage, Vijayaraghavan Rajagopal, J. Jane Cao, Poul M. F. Nielsen, Chris P. Bradley, Alistair A. Young, and Martyn P. Nash. Efficient estimation of load-free left ventricular geometry and passive myocardial properties using principal component analysis. *International Journal for Numerical Methods in Biomedical Engineering*, n/a(n/a):e3313, 2020.

[66] Ken CL Wong, Jatin Relan, Linwei Wang, Maxime Sermesant, Hervé Delingette, Nicholas Ayache, and Pengcheng Shi. Strain-based regional nonlinear cardiac material properties estimation from medical images. In *International Conference on Medical Image Computing and Computer-Assisted Intervention*, pages 617–624. Springer, 2012.

[67] Jia Wu, Katharine G. Brigham, Marc A. Simon, and John C. Brigham. An implementation of independent component analysis for 3d statistical shape analysis. *Biomedical Signal Processing and Control*, 13:345–356, sep 2014.

[68] Jia Wu, Marc A. Simon, and John C. Brigham. A comparative analysis of global shape analysis methods for the assessment of the human right ventricle. *Computer Methods in Biomechanics and Biomedical Engineering: Imaging & Visualization*, 4(6):327–343, jul 2014.

[69] Jia Wu, Yingqian Wang, Marc A Simon, and John C Brigham. A new approach to kinematic feature extraction from the human right ventricle for classification of hypertension: a feasibility study. *Physics in Medicine & Biology*, 57(23):7905, 2012.

[70] Jia Wu, Yingqian Wang, Marc A. Simon, Michael S. Sacks, and John C. Brigham. A new computational framework for anatomically consistent 3d statistical shape analysis with clinical imaging applications. *Computer Methods in Biomechanics and Biomedical Engineering: Imaging & Visualization*, 1(1):13–27, mar 2013.

[71] Jing Xu, Marc A Simon, Timothy C Wong, and John C Brigham. A shape analysis based strategy for estimation of in vivo ventricular wall elasticity. Zeta Computational Resources Ltd., 2017.

[72] Huina Yuan, Bojan B. Guzina, and Ralph Sinkus. Application of topological sensitivity toward tissue elasticity imaging using magnetic resonance data. *Journal of Engineering Mechanics*, 140(3):443–453, 2014.

[73] Dengsheng Zhang and Guojun Lu. Review of shape representation and description techniques. *Pattern recognition*, 37(1):1–19, 2004.